

# Scaling Enhancement in Distributed Quantum Sensing via Causal Order Switching

Binke Xia,<sup>1</sup> Zhaotong Cui,<sup>2</sup> Jingzheng Huang,<sup>2,3,4,\*</sup> Yuxiang Yang,<sup>1,†</sup> and Guihua Zeng<sup>2,3,4,‡</sup>

<sup>1</sup>*QICI Quantum Information and Computation Initiative, School of Computing and Data Science, The University of Hong Kong, Pokfulam Road, Hong Kong, China*

<sup>2</sup>*State Key Laboratory of Photonics and Communications, Institute for Quantum Sensing and Information Processing,*

*School of Automation and Intelligent Sensing, Shanghai Jiao Tong University, Shanghai 200240, China*

<sup>3</sup>*Hefei National Laboratory, Hefei 230088, China*

<sup>4</sup>*Shanghai Research Center for Quantum Sciences, Shanghai 201315, China*

(Dated: January 22, 2026)

Sensing networks underpin applications from fundamental physics to real-world engineering. Recently, distributed quantum sensing (DQS) has been investigated to boost the sensing performance, yet current schemes typically rely on entangled probes that are fragile to noise and difficult to scale. Here, we propose a DQS protocol that incorporates a causal-order switch into a cyclic network, enabling a single probe to sequentially query  $N$  independent sensors in a coherent superposition or a probabilistic mixture of opposite causal orders. By exploiting the noncommutativity between propagation and sensing processes, our scheme achieves a  $1/N^2$ -scaling precision limit without involving entangled probes. Importantly, our approach utilizes a classical mixture of causal orders rather than a quantum switch, making it more feasible for practical realization. We experimentally implement this scheme for distributed beam tilts sensing in a free-space quantum optical network comprising up to 9 sensors, achieving picoradian-scale precision in estimating tilt angle. Our results demonstrate a robust and scalable DQS protocol that surpasses the conventional  $1/N$  Heisenberg scaling in precision, advancing the practical deployment of quantum sensing networks.

## I. INTRODUCTION

Quantum sensing has demonstrated capabilities of achieving higher sensitivity and precision beyond the classical counterparts [1], and has been applied to various scenarios ranging from gravitational wave detection [2–4], navigation technologies [5–7], biochemical applications [8, 9], and materials science [10, 11]. Yet most demonstrations target a single parameter at a single location. By contrast, networking spatially distributed sensors is increasingly recognized as critical for the practical, real-world deployment of quantum sensing technologies.

Generally, a sensing network involves  $N$  independent parameters which are encoded at  $N$  spatially separated sensors, and a global parameter, typically the average of these local parameters, is finally estimated [12, 13]. In classical distributed sensing scenarios, each sensor employs a localized probe and operates independently, so the precision in estimating the global is proportional to  $1/\sqrt{N}$ , the standard-quantum limit (SQL) [12, 13].

Recently, theoretical works [14–18] have demonstrated that distributed quantum sensing (DQS), where multiple sensors share entangled probes, can improve the sensing performance and even achieve the Heisenberg limit (HL)  $1/N$  in estimating the global parameter. Experimentally, realizations of quantum-enhanced distributed sensing have so far relied on non-classical states of light. For instance, Greenberger–Horne–Zeilinger (GHZ) polarization-entangled photon states have been employed for distributed phase sensing in discrete-variable (DV) platforms [19–22], whereas continuous-variable (CV) multipartite entanglement generated from squeezed light has enabled distributed sensing of phase-space displacements [23], radio-frequency signals [24], and forces [25]. While these works demonstrate precision beyond the SQL  $1/\sqrt{N}$ , and even achieve the HL  $1/N$ , current implementations involve no more than 6 nodes in DV systems and 4 nodes in CV systems, primarily due to challenges in generating large-scale entanglement [26–28] and the fragility of non-classical probes [29, 30], thereby constraining practical deployment. Moreover, whether enhancement scalings beyond  $1/N$  can be achieved in DQS remains an open question, even though such scalings have already been observed in certain single-parameter quantum metrological scenarios [31–35].

Rather than parallelly distributing entangled probes across multiple sensors, here we consider a cyclic network in which a server node prepares a single probe that queries multiple sensors sequentially before a final measurement at the server. In principle, the sequential strategy has been demonstrated the capability of achieving the HL for single-parameter estimation at a single location [36, 37]. While in realistic quantum sensing networks, the probe

\* jzhuang1983@sjtu.edu.cn

† yxyang@hku.hk

‡ gzheng@sjtu.edu.cn

must propagate between spatially separated sensors, and propagation effects generally degrade the ultimate precision [38–40]. However, the noncommutativity between propagation and sensing processes is itself an important quantum resource [41–43]. Previous quantum metrological schemes have exploited this resource by employing the quantum strategy called “indefinite causal order” [34, 44], which leverages the noncommutativity of different quantum gates. This approach has been shown to outperform both sequential and parallel strategies in quantum metrology [45], and can even achieve a “super-Heisenberg” scaling ( $\propto 1/N^2$ ) in estimating a global geometric phase [34, 35]. Nevertheless, these schemes rely on a quantum switch [46] to combine quantum processes in a coherent superposition of alternative orders. In this work, we instead incorporate a causal-order-switching strategy directly into the network architecture by employing an external switch ancilla. In contrast to the indefinite-causal-order strategy, our approach does not require the ancilla to be initialized in a pure quantum state. Rather, our scheme allows for a classical ancilla, represented by a probabilistic mixture, so that the probe sequentially queries the  $N$  sensors in a probabilistic mixture of opposite causal orders. Our theoretical result shows that this mixture of pure strategies outperforms each individual pure strategy, which is rare in quantum metrology.

To implement causal order switching in our cyclic sensing network, we use the photon’s polarization as a switch ancilla, enabling either a coherent superposition or a probabilistic mixture of opposite propagation directions for the probe. Specifically, we investigate the distributed sensing of transverse momentum kicks on a quantum probe, which generally correspond to beam tilts [47, 48] in free-space quantum optical networks. In this scenario, the quantum processes associated with momentum kick and free-space propagation do not commute, inducing an additional space shift of the probe state. By allowing the probe to sequentially query all sensors in a coherent superposition or a probabilistic mixture of opposite causal orders, the average momentum kick is mapped directly onto the additional space shift of the final probe and is amplified by a factor containing an  $N^2$  term, yielding a  $1/N^2$ -scaling enhancement in the ultimate precision limit of estimating the global sensing parameter. We experimentally demonstrate this nonlinear-scaling enhancement for distributed beam tilts sensing in a free-space quantum optical network. In our experiments, we further employ the weak value amplification (WVA) technique to improve practical precision [49]. By implementing a cyclic network with up to 9 sensors, we achieve prad-scale precision in estimating the average tilt angle. Consequently, our findings shed new light on the practical deployment of quantum sensing networks, and the demonstrated prad-scale beam-tilt sensitivity is relevant to various applications like interferometric alignment, vibration monitoring, and acoustic sensing.

## II. RESULTS

First, we investigate the distributed quantum sensing within a cyclic network, as depicted in Fig. 1. The network consists of a server node and  $N$  sensing nodes. An initial probe state  $|\psi_i\rangle$  is prepared at the server node and sent through sensors within the network. Then the final probe state  $|\psi_f\rangle$  is measured at the server node to estimate the average value  $\bar{\theta} = \frac{1}{N} \sum_{j=1}^N \theta_j$  of the unknown parameters  $\boldsymbol{\theta} = (\theta_1, \theta_2, \dots, \theta_N)$  across the sensing network. In general, we assume that all  $N$  sensors are identical, i.e., each sensing node is associated with the same Hamiltonian, denoted by  $\hat{H}_S$ . The  $j$ -th sensing node encodes its respective unknown parameter  $\theta_j$  onto the probe state via a unitary process  $\hat{U}_{\theta_j} = \exp[-i\hat{H}_S\theta_j]$ .

Typically, existing schemes of distributed quantum sensing [13] considered star-type networks that distribute the probe state to all sensors in parallel. Here, instead, we consider a cyclic network, which allows the prepared probe state to query all  $N$  sensors sequentially. As depicted in Fig. 1a, the probe state queries the sensors in a fixed causal order, as in the sequential quantum metrological scheme, the ultimate precision in estimating the parameter  $\bar{\theta}$  scales linearly with the number  $N$  of sensors, i.e.,  $\delta\bar{\theta}_{\min} \propto 1/N$ . In realistic sensing networks, however, one must also account for the free propagation of the probe between nodes. In this work, we investigate the propagation process that can be described via a unitary operator  $\hat{U}_z = \exp[-i\hat{H}_P z]$  (or  $\hat{U}_t = \exp[-i\hat{H}_P t]$ ), where  $z$  (or  $t$ ) denotes the propagation distance (or time) and  $\hat{H}_P$  is the propagation Hamiltonian. Theoretically, the achievable precision may degrade when  $\hat{H}_P$  fails to commute with the sensing Hamiltonian, i.e.,  $[\hat{H}_P, \hat{H}_S] \neq 0$ , since the noncommutative evolution may carry the probe away from the optimal state for sensing. By contrast, if the probe state queries the sensors in a superposition of different causal orders, the interplay between propagation and sensing can be exploited to further enhance precision—potentially surpassing the linear Heisenberg scaling.

To be clear, we investigate a free-space quantum optical sensing scenario. In this context, the sensing process at each sensor is described by a unitary evolution  $\hat{U}_\theta = \exp(-i\theta\hat{X})$ , which leads to a momentum kick  $\theta$  on the probe state. In practice, this is typically implemented via an angular tilt of the light beam. The free-space propagation between nodes is described by the unitary operator  $\hat{U}_z = \exp(-iz\hat{P}^2/2k)$ , where  $k$  denotes the wave number and  $z$  is the propagation distance. This sensing scenario is relevant to a variety of practical applications, such as optical path alignment, vibration sensing, and acoustic sensing. We denote the distances between consecutive nodes as  $z_0, z_2,$

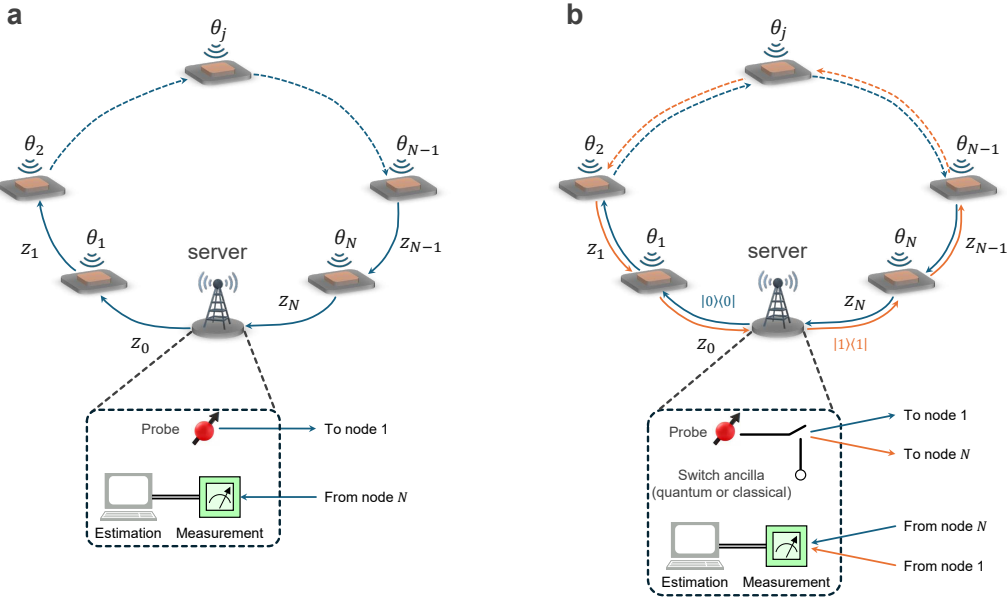


FIG. 1. Schematic of distributed quantum sensing within a cyclic network. **a** Probe state sequentially queries  $N$  sensing nodes in a fixed causal order. **b** Probe state sequentially queries  $N$  sensing nodes in a coherent superposition or a probabilistic mixture of opposite causal orders. An external ancilla, realized either as a qubit (quantum switch) or as a probabilistic mixed state (classical switch), is employed to control the causal order of the probe within the network. The probe state is prepared and the final measurement is performed in the server node.

$\dots, z_N$ , where  $z_0$  is the distance from the server node to the first sensor and  $z_N$  is the distance from the last sensor back to the server node. Accordingly, the total evolution of the probe state throughout the sensing network within a fixed causal order can be expressed as  $\hat{U}(\theta) = \hat{U}_+ = \hat{U}_{z_N} \hat{U}_{\theta_N} \dots \hat{U}_{\theta_2} \hat{U}_{z_1} \hat{U}_{\theta_1} \hat{U}_{z_0}$ . In this case, we can show that the quantum precision limit for estimating the global average  $\bar{\theta}$  exhibits Heisenberg scaling, i.e.,  $\delta\bar{\theta}_{\text{QL}} \propto 1/N$ . (See the Supplemental Materials for details of proof.)

Subsequently, we consider the probe state passing through this network in a superposition (or a mixture) of opposite causal orders, where the evolution corresponding to the reverse causal order is given by  $\hat{U}_- = \hat{U}_{z_0} \hat{U}_{\theta_1} \hat{U}_{z_1} \hat{U}_{\theta_2} \dots \hat{U}_{\theta_N} \hat{U}_{z_N}$ . As depicted in Fig. 1b, a switch ancilla is employed to control the causal order of the probe within the network, with the state  $|0\rangle\langle 0|$  selecting the forward propagation and  $|1\rangle\langle 1|$  selecting the backward propagation. Then the joint evolution of the probe and the ancilla with causal order switching is given by

$$\begin{aligned} \hat{U}(\theta) &= \hat{U}_+ \otimes |0\rangle\langle 0| + \hat{U}_- \otimes |1\rangle\langle 1| \\ &= \exp\left[-i\frac{g_1^2 - g_2^2}{4k(N+1)\bar{z}}\right] \exp\left[-i\frac{(N+1)\bar{z}}{2k}\hat{P}^2\right] \exp\left(-i\frac{g_1}{k}\hat{P}\right) \exp\left[-i\frac{g_1 + g_2}{(N+1)\bar{z}}\hat{X}\right] \otimes |0\rangle\langle 0| \\ &\quad + \exp\left[i\frac{g_1^2 - g_2^2}{4k(N+1)\bar{z}}\right] \exp\left[-i\frac{(N+1)\bar{z}}{2k}\hat{P}^2\right] \exp\left(-i\frac{g_2}{k}\hat{P}\right) \exp\left[-i\frac{g_1 + g_2}{(N+1)\bar{z}}\hat{X}\right] \otimes |1\rangle\langle 1|, \end{aligned} \quad (1)$$

where  $\bar{z} = \frac{1}{N+1} \sum_{j=0}^N z_j$  denotes the average propagation distance between adjacent sensors, and

$$g_1 = \sum_{j=0}^{N-1} z_j \left( \sum_{l=j+1}^N \theta_l \right), \quad g_2 = \sum_{j=1}^N z_j \left( \sum_{l=1}^j \theta_l \right), \quad g_1 + g_2 = (N+1)N\bar{z}\bar{\theta}. \quad (2)$$

Here, the switch ancilla can be either a pure qubit (quantum switch), initialized as  $|\phi_{\text{sw}}\rangle = (|0\rangle + |1\rangle)/\sqrt{2}$ , or a probabilistic mixed state (classical switch), initialized as  $\hat{\rho}_{\text{sw}} = (|0\rangle\langle 0| + |1\rangle\langle 1|)/2$ . The quantum switch enables a coherent superposition of opposite causal orders of the probe within the network, whereas the classical switch implements a probabilistic mixture of these opposite causal orders.

It can be seen that the joint evolution within our sensing network encodes the two parameters,  $g_1$  and  $g_2$ , into the probe state. The average value of the parameter of interest,  $\bar{\theta}$ , is simply the sum of these two parameters. Therefore, estimating  $\bar{\theta}$  is equivalent to estimating a function of  $g_1$  and  $g_2$ . Theoretically, the ultimate precision limit

for estimating  $\bar{\theta}$  is determined by the quantum Cramér-Rao bound (QCRB), which can be derived from the quantum Fisher information matrix (QFIM) associated with the parameters  $g_1$  and  $g_2$ , and is given by

$$\mathcal{C}_{\bar{\theta}} = G [\mathcal{Q}(g_1, g_2)]^{-1} G^T, \quad (3)$$

where  $\mathcal{Q}(g_1, g_2)$  denotes the corresponding QFIM of simultaneously estimating  $g_1$  and  $g_2$  from the final joint state of the probe and the ancilla, and  $G = (\partial_{g_1} \bar{\theta}, \partial_{g_2} \bar{\theta})$  is the associated Jacobian matrix. With a quantum switch, the final joint state  $|\Psi_f^{(qCW)}\rangle = \hat{U}(\boldsymbol{\theta})|\psi_i\rangle \otimes |\phi_{\text{SW}}\rangle$  is pure, whereas with a classical switch, the final joint state  $\hat{\rho}_f^{(cSW)} = \hat{U}(\boldsymbol{\theta})(|\psi_i\rangle\langle\psi_i| \otimes \hat{\rho}_{\text{SW}})\hat{U}^\dagger(\boldsymbol{\theta})$  is a probabilistic mixture. However, whether employing a quantum switch or a classical switch, the QCRB for estimating the global average  $\bar{\theta}$  exhibits a “super-Heisenberg” scaling (Detailed calculations of the QFIMs  $\mathcal{Q}^{(qSW)}(g_1, g_2)$  and  $\mathcal{Q}^{(cSW)}(g_1, g_2)$ , as well as the corresponding QCRBs  $\mathcal{C}_{\bar{\theta}}^{(qSW)}$  and  $\mathcal{C}_{\bar{\theta}}^{(cSW)}$ , are provided in the Supplemental Materials.)

$$\lim_{N \rightarrow \infty} \mathcal{C}_{\bar{\theta}}^{(qSW)}/N^{-4} = \lim_{N \rightarrow \infty} \mathcal{C}_{\bar{\theta}}^{(cSW)}/N^{-4} = \frac{k^2}{\bar{z}^2 \langle \Delta \hat{P}^2 \rangle_i}, \quad (4)$$

where  $\langle \Delta \hat{P}^2 \rangle_i = \langle \psi_i | \hat{P}^2 | \psi_i \rangle - \langle \psi_i | \hat{P} | \psi_i \rangle^2$  is the momentum variance on the initial probe state  $|\psi_i\rangle$ .

Theoretically, the QCRB  $\mathcal{C}_{\bar{\theta}}$  is achievable through optimal measurements in single-parameter estimation scenarios. Consequently, the quantum precision limit on estimating the parameter  $\bar{\theta}$  is given by  $\delta\bar{\theta}_{\text{QL}} = \sqrt{\nu \mathcal{C}_{\bar{\theta}}}$ , where  $\nu$  denotes the number of independent trials. Drawing on Eq. (4), we can conclude that this quantum precision limit satisfies

$$\lim_{N \rightarrow \infty} \delta\bar{\theta}_{\text{QL}}/N^{-2} = \frac{k}{\sqrt{\nu \bar{z} \Delta P_i}}, \quad (5)$$

where  $\Delta P_i = \sqrt{\langle \Delta \hat{P}^2 \rangle_i}$  is the momentum uncertainty of the initial probe state. This result implies that a “super-Heisenberg” scaling enhancement,  $\delta\bar{\theta}_{\text{QL}} \propto 1/N^2$ , can be practically achieved by implementing either a coherent superposition or a probabilistic mixture of opposite causal orders into the cyclic quantum sensing network.

Importantly, this nonlinear enhancement does not depend on mode entanglement between different sensors. Instead, it arises from the noncommutativity between the sensing process and the natural propagation process, as well as the mixture of causal orders. These factors collectively contribute to the significant advantages observed in our scheme. In this context, the coherence of the probe state is crucial for the successful implementation of our scheme. Consequently, unlike distributed quantum sensing protocols that rely on multipartite entanglement, our approach can be realized using coherent light sources, and the nonlinear-scaling enhancement remains observable even in the presence of classical noises.

For practical demonstration, we design an experimental scheme as illustrated in Fig. 2. In our experiments, the sensing parameter  $\theta_j$  is defined as a momentum kick encoded in the  $j$ -th sensing node, which can be implemented by introducing a tiny angular tilt to the light beam in an optical system. Consequently, we choose the probe state to be the transverse mode of the light beam, which is initially prepared in a Gaussian profile and denoted as

$$|\psi_i\rangle = \int dx \psi(x) |x\rangle, \quad \psi_i(x) = \left( \sqrt{\frac{\pi}{2}} w_0 \right)^{-\frac{1}{2}} \exp \left( -\frac{x^2}{w_0^2} \right), \quad (6)$$

where  $\psi_i(x)$  is the wave function of initial probe state and  $w_0 = 2\Delta X_i = 1/\Delta P_i$  is the radius of beam waist. Meanwhile, we choose the ancilla to the polarization state of the light beam, which is initialized as a  $45^\circ$  linear polarized state  $|\phi_{\text{SW}}\rangle = |i\rangle = (|H\rangle + |V\rangle)/\sqrt{2}$ . Notably, although we employ a pure state as the switch ancilla, our theory does not require the ancilla to be in a pure state. This choice is motivated by practical considerations: first, the polarization of coherent light is typically fixed; second, a pure-state ancilla enables the utilization of the weak value amplification (WVA) technique, which can further suppress classical noise and improve the sensitivity in estimating the unknown parameter.

For practical implementation, we apply the parity operation to the reverse propagation branch, which can be physically realized by incorporating mirrors within the free-space optical sensing network. Consequently, the joint evolution of the probe and the ancilla can be represented as  $\hat{U}_+ \otimes |H\rangle\langle H| + \hat{\pi}^\dagger \hat{U}_- \hat{\pi} \otimes |V\rangle\langle V|$ , where  $\hat{\pi}$  denotes the parity operator, satisfying  $\hat{\pi}^\dagger \hat{X} \hat{\pi} = -\hat{X}$  and  $\hat{\pi}^\dagger \hat{P} \hat{\pi} = -\hat{P}$ . In addition, the propagation distances  $z_{\text{in}}$  (from the initial probe state at the beam waist to the input of the network) and  $z_{\text{out}}$  (from the output of the network to the measurement terminal) must be taken into account. These introduce additional propagation evolutions, denoted as  $\hat{U}_{z_{\text{in}}}$  and  $\hat{U}_{z_{\text{out}}}$ , acting on the probe state before entering and after exiting the sensing network, respectively. To implement the WVA technique within our experimental scheme, we ensure that the parameters  $\bar{\theta} \ll 1$ ,  $g_1 \ll 1$  and  $g_2 \ll 1$  are maintained

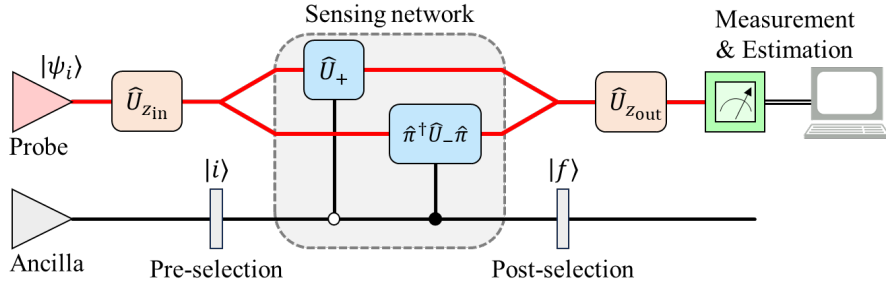


FIG. 2. Schematic of the experimental scheme with weak value amplification. The ancilla is prepared in the pre-selected state  $|i\rangle$ , which creates a coherent superposition of opposite causal orders for the probe within the cyclic network. A parity operation is applied to the reverse-propagation branch, and the ancilla is subsequently projected onto the post-selected state  $|f\rangle$ , thereby realizing weak value amplification.

throughout the experiments. Under these conditions, the joint evolution of the probe and the ancilla in our scheme can be expressed as:

$$\begin{aligned} \hat{U}_{\text{exp}} &= \hat{U}_{z_{\text{out}}} \hat{U}_{z_{\text{in}}} \otimes |H\rangle\langle H| + \hat{U}_{z_{\text{out}}} \hat{\pi}^\dagger \hat{U}_- \hat{\pi} \hat{U}_{z_{\text{in}}} \otimes |V\rangle\langle V| \\ &\approx \left( \hat{U}_{z_{\text{tot}}} \otimes \hat{\mathbb{I}} \right) \left\{ \hat{\mathbb{I}} - i \left[ \frac{\bar{z}}{2k} N^2 \bar{\theta} + \left( \frac{\bar{z}}{2k} + \frac{z_{\text{in}}}{k} \right) N \bar{\theta} \right] \hat{P} \otimes \hat{A} - i \frac{g_1 - g_2}{2k} \hat{P} \otimes \hat{\mathbb{I}} - i N \bar{\theta} \hat{X} \otimes \hat{A} \right\}, \end{aligned} \quad (7)$$

where  $\hat{A} = |H\rangle\langle H| - |V\rangle\langle V|$  is a Pauli operator,  $z_{\text{tot}} = z_{\text{in}} + (N+1)\bar{z} + z_{\text{out}}$  denotes the total propagation distance of the probe. It can be seen that the momentum kicks  $\theta_1, \theta_2, \dots, \theta_N$  induce a nonlinear spatial displacement of  $(\bar{z}/2k)N^2\bar{\theta}$  in the probe state, which arise from the noncommutativity between the momentum kick and the free-space propagation.

Subsequently, by post-selecting the ancilla to a final state  $|f\rangle = (e^{-i\varepsilon}|H\rangle - e^{i\varepsilon}|V\rangle)/\sqrt{2}$ , we can derive the final probe state as

$$|\psi_f\rangle = \frac{\langle f | \hat{U}_{\text{exp}} | i \rangle |\psi_i\rangle}{\| \langle f | \hat{U}_{\text{exp}} | i \rangle |\psi_i\rangle \|} \approx \mathcal{N}_f \hat{U}_{z_{\text{tot}}} \left\{ \hat{\mathbb{I}} - i A_w \left[ \frac{\bar{z}}{2k} N^2 \bar{\theta} + \left( \frac{\bar{z}}{2k} + \frac{z_{\text{in}}}{k} \right) N \bar{\theta} \right] \hat{P} - i \frac{g_1 - g_2}{2k} \hat{P} - i A_w N \bar{\theta} \hat{X} \right\} |\psi_i\rangle, \quad (8)$$

where  $\mathcal{N}_f = \langle f | i \rangle / \| \langle f | \hat{U}_{\text{exp}} | i \rangle |\psi_i\rangle \|$  is the normalization factor,  $\| \langle f | \hat{U}_{\text{exp}} | i \rangle |\psi_i\rangle \|^2$  is the success probability of post-selection and

$$A_w = \frac{\langle f | \hat{A} | i \rangle}{\langle f | i \rangle} = i \cot \varepsilon \approx i \frac{1}{\varepsilon} \quad (9)$$

is the weak value. Theoretically, this imaginary weak value transforms the nonlinear spatial displacement of the probe state into a nonlinear momentum shift. As a result, the amplified signal can be extracted through a transverse momentum measurement on the final probe state. In practice, this can be implemented in an optical system by employing a Fourier lens and positioning a quadcell photodetector (QPD) at its focal plane. Theoretically, the corresponding measurement operator is given by

$$\hat{M} = \hat{U}_f^\dagger \hat{U}_{z=f}^\dagger \hat{X} \hat{U}_{z=f} \hat{U}_f = \frac{f}{k} \hat{P}, \quad (10)$$

where  $\hat{U}_f = \exp(-ik\hat{X}^2/2f)$  is the quadratic phase front given by the Fourier lens,  $f$  is the focal length and  $\hat{U}_{z=f} = \exp(-if\hat{P}^2/2k)$  denotes the propagation from the lens to the QPD. Therefore, this setup measures the average momentum of the final probe state, and the mean value and standard deviation of this measurement can be calculated separately as

$$\bar{M}_f = \langle \hat{M} \rangle_f \approx \frac{2f}{k\varepsilon} \langle \Delta \hat{P}^2 \rangle_i \left[ \frac{\bar{z}}{2k} N^2 + \left( \frac{\bar{z}}{2k} + \frac{z_{\text{in}}}{k} \right) N \right] \bar{\theta}, \quad (11)$$

$$\Delta M_f = \sqrt{\langle \Delta \hat{M}^2 \rangle_f} \approx \frac{f}{k} \Delta P_i. \quad (12)$$

Theoretically, the minimum detectable value of  $\bar{\theta}$  in a single-shot measurement is obtained when  $\bar{M}_f = \Delta M_f$  and is given as

$$\delta \bar{\theta}_{\text{min}} = \frac{k\varepsilon}{\bar{z} \Delta P_i} \cdot \frac{1}{N^2 + (1 + 2z_{\text{in}}/\bar{z}) N}. \quad (13)$$

Therefore, our experimental scheme yields a nonlinear-enhanced-scaling precision limit  $\delta\bar{\theta}_{\min} \propto 1/[N^2 + (1 + 2z_{\text{in}}/\bar{z})N]$  in estimating the parameter  $\bar{\theta}$ .

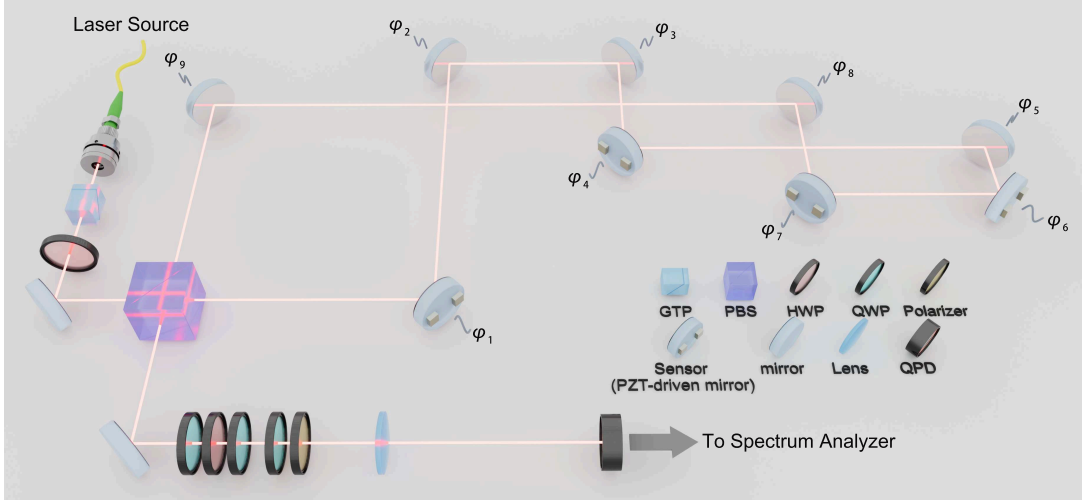


FIG. 3. Experimental setup. A 780 nm laser beam is coupled into free space using a collimator. The polarization (ancilla) is initialized with a Glan–Taylor polarizer (GTP) and a half-wave plate (HWP). The cyclic sensing network with a coherent superposition of opposite causal orders is realized in a polarizing Sagnac interferometer, where PZT-driven mirrors inside the interferometer serve as the sensors. The number of sensors is set by adjusting the loops and mirrors in the Sagnac interferometer; here we illustrate a configuration with 9 sensors. The final polarization state is post-selected by a polarizer combining with a quarter-wave plate (QWP) to implement the weak value amplification. A Fourier lens and a quadcell photodetector (QPD) are used to measure the transverse momentum of the final probe state.

Experimentally, we construct the sensing network using a Sagnac interferometer, in which the horizontally polarized component  $|H\rangle$  and the vertically polarized component  $|V\rangle$  of light propagate in opposite directions. The schematic of our experimental setup is illustrated in Fig. 3, where 9 sensors are integrated, and the number of sensors in the network can be reconfigured by changing the number of loops in the Sagnac interferometer (see the Supplemental Materials for details). Mirrors driven by piezoelectric transducer (PZT) chips are utilized to generate tiny angular tilts in the light beam; specifically, a tilt angle  $\varphi_j$  is applied at the  $j$ -th sensing node, resulting in a transverse momentum kick  $\theta_j = k\varphi_j$  encoded onto the probe state. The interferometer is constructed using an odd number of mirrors (including both PZT-driven and non-driven mirrors), which ensures a parity transformation with respect to the reverse propagation direction of the probe state within the network. This design is essential for the implementation of the weak value amplification (WVA) method in our experiment.

The initial ancilla state  $|i\rangle$  is prepared using a linear polarizer and a half-wave plate (HWP), while the post-selection state  $|f\rangle$  is realized with a quarter-wave plate (QWP) and an additional linear polarizer. In our experiments, the post-selection angle  $\varepsilon$  is adjusted by rotating the linear polarizer to achieve a fixed weak value of  $|A_w| \approx 7$ . Furthermore, a “sandwich” configuration consisting of two QWPs and one HWP is employed to compensate for the additional relative phase introduced by the interferometer. (Details on the principles and explicit configurations of these wave plates are provided in the Supplemental Materials.)

In our experiments, the differential intensity  $I_\Delta$ , which is defined as the difference between the detected intensity  $I_L$  on the left half and  $I_R$  on the right half of the QPD, determines the central position of the final received beam. Therefore, the measured value of  $\bar{M}_f$  is given by  $I_\Delta$  in our experiments. Specifically, the QPD we used provides the relation  $\bar{M}_f = 0.65(I_\Delta/I_0) \times \text{beam radius}$  to obtain the detected beam position, where  $I_0 = I_L + I_R$  is the total intensity received by the QPD, and the received beam radius on the QPD is  $2\Delta M_f \approx (2f/k)\Delta P_i = 2f/w_0k$ . Thus, the directly measured signal  $I_\Delta$  on the QPD allows us to determine the value of the sensing parameter  $\bar{\theta}$  via the relation

$$\begin{aligned} I_\Delta &= \frac{2I_0}{1.3\varepsilon w_0} \left[ \frac{\bar{z}}{2k} N^2 + \left( \frac{\bar{z}}{2k} + \frac{z_{\text{in}}}{k} \right) N \right] \bar{\theta} \\ &= \frac{\bar{z}I_0}{1.3\varepsilon w_0} \left[ N^2 + \left( 1 + \frac{2z_{\text{in}}}{\bar{z}} \right) N \right] \bar{\varphi}, \end{aligned} \quad (14)$$

where  $\bar{\varphi}$  is the average value of tilt angles introduced on each sensing nodes in this network.

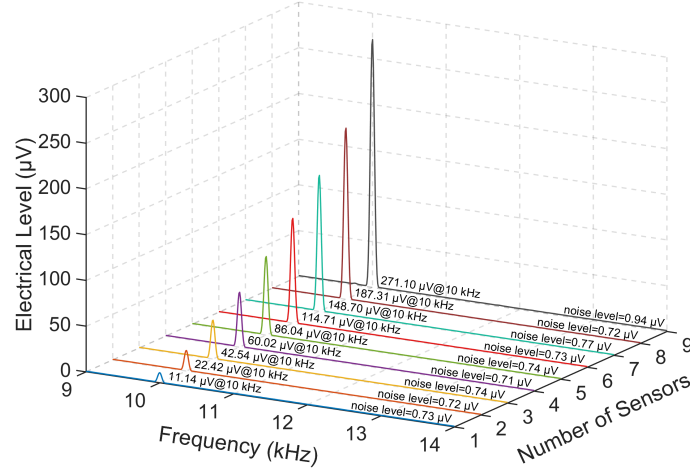


FIG. 4. Detected spectrums for 1 to 9 sensors. 5 mV peak-to-peak driving signals are synchronously applied to the PZT chips of sensors, which corresponds an 11 nrad beam-tilt modulation in each sensor. The frequency of applied signals is set at 10 kHz.

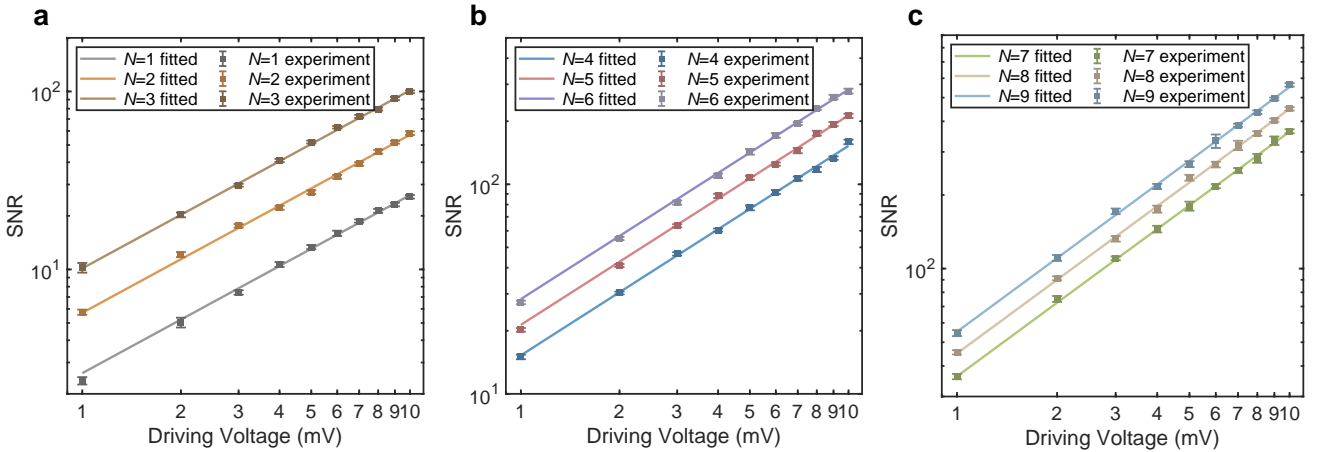


FIG. 5. Experimental results of detected signal-to-noise ratio (SNR) at the spectrum analyzer. The applied peak-to-peak voltage is varied from 1 mV to 10 mV in 1 mV increments, corresponding to a loaded average tilt signal from 2.2 nrad to 22 nrad in 2.2 nrad increments. **a** Experimental results of 1 to 3 sensors configured in the network. **b** Experimental results of 4 to 6 sensors configured in the network. **c** Experimental results of 7 to 9 sensors configured in the network. Square markers with error bars stand for the measured SNR; solid lines represent fits to the experimental data.

We stabilized the received optical power  $I_0$  on the QPD at approximately 0.2 mW. Synchronized 10 kHz sinusoidal drive signals from waveform generators were applied to the PZT chips to produce synchronized tilt modulation at each sensing node. A 5 mV peak-to-peak drive corresponded to an 11 nrad beam-tilt modulation (see the Methods section for details). The QPD then converted the differential optical power  $I_\Delta$  into an electrical signal, which was fed to a spectrum analyzer to extract the 10 kHz component corresponding to the average tilt  $\bar{\varphi}$ .

Fig. 4 shows the amplitude spectrums of the QPD differential signal for configurations with 1 to 9 sensors. The synchronized PZT drive amplitude was fixed at 5 mV peak-to-peak voltage. The peak levels at 10 kHz arise from the tilt signals  $\bar{\varphi}$  and increase nonlinearly with the number of sensors. From these spectrums we also estimate the noise floor and hence the peak signal-to-noise ratio (SNR), which we use to determine the minimum detectable angular tilt  $\delta\bar{\varphi}_{\min}$ . Because a continuous-wave coherent laser was used as the light source, the measured noise floor includes not only shot noise but also classical (technical) noises such as thermal, relative-intensity, and electronic noise. In practice, these contributions are approximately independent of the number of sensors. Accordingly, the minimum detectable tilt in our experiments satisfies (see the Methods section for a detailed analysis)

$$\delta\bar{\varphi}_{\min} \propto \frac{1}{N^2 + (1 + 2z_{\text{in}}/\bar{z})N}, \quad (15)$$

which is improved nonlinearly with the number  $N$  of sensors.

To experimentally determine the minimum detectable angular tilt angle  $\delta\bar{\varphi}_{\min}$  for different numbers of sensors, we synchronously varied the driving voltage applied to the PZT chips from 1 mV to 10 mV in 1 mV increments, corresponding to a loaded average tilt signal from 2.2 nrad to 22 nrad in 2.2 nrad increments. In our experiments, the number of sensors was increased from 1 to 9 in increments of 1 by reconfiguring the Sagnac interferometer. For each number of sensors and each voltage setting, we acquired 100 measurements of the spectral peak level and the noise-floor level from the spectrum analyzer, calculated the SNR for each measurement (see Supplemental Materials for details), and plotted the mean SNR with error bars versus driving voltage for each number of sensors in Fig. 5. Since the spectrum analyzer's noise floor is independent of the tilt signal, the SNR is expected to scale linearly with the applied voltage. Accordingly, we fit a linear relation to SNR versus driving voltage for each number of sensors in Fig. 5. From the fitted lines, we can infer the driving voltage corresponding to  $\text{SNR} = 1$  and converted it to the corresponding minimum detectable average tilt angle,  $\delta\bar{\varphi}_{\min}$ , for each number of sensors.

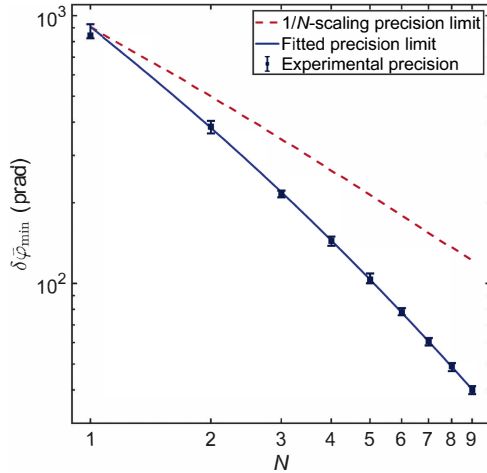


FIG. 6. Experimental results of measurement precision for the average tilt angle  $\bar{\varphi}$  as a function of the number of sensors (1 to 9) configured in the network. Square markers with error bars stand for the measured precision. The blue solid line is a nonlinear fit (precision vs. sensor count) to the experimental data. The red dashed line shows the precision limit expected under linear improvement.

In Fig. 6, We illustrate the experimental results of the minimum detectable average tilt angle  $\delta\bar{\varphi}_{\min}$  for number of sensors from 1 to 9. These results indicate that we achieve picoradian-scale sensitivity (see the Supplemental Materials for detailed results). According to Eq. (15), we fit the dependence of  $\delta\bar{\varphi}_{\min}$  on the number  $N$  of sensors, obtaining a precision limit  $\delta\bar{\varphi}_{\min} \approx 4.77/(N^2 + 4.25N)$  nrad from the experimental data; the fitted precision limit is also shown in Fig. 6. Notably, our goodness of fit is high (coefficient of determination  $R^2 = 99.18\%$ ), indicating that the observed nonlinear-scaling enhancement with  $N$  is well captured by Eq. (15). For comparison, we also plot a  $1/N$ -scaling precision limit in Fig. 6 by replacing the  $N^2$  term with 1 in our fitted relation between  $\delta\bar{\varphi}_{\min}$  and  $N$ . This linear-scaling limit is known as the Heisenberg limit, long regarded as the ultimate precision limit in quantum-enhanced distributed sensing. Our experimental results clearly show that our scheme achieves a precision beyond Heisenberg scaling for quantum-enhanced distributed sensing. Importantly, this enhancement does not rely on entangled probes and remains robust in the presence of classical noise.

### III. DISCUSSION

In this work, we implemented the final readout of the probe state using WVA technique. WVA has been shown to be effective at suppressing technical noises [49]. In particular, realizing an imaginary weak value enables direct measurement in the probe's transverse-momentum space to extract the global-averaged sensing parameter, thereby circumventing the effects of spatial dispersion accumulated during free-space propagation. While our experimental realization requires the ancilla to be initialized in a pure state, and employs an additional parity operation on the reverse-propagation branch of the sensing network together with post-selection on the ancilla to realize WVA, our theoretical framework does not rely on these steps to achieve the nonlinear-scaling precision enhancement. In the absence of WVA, however, the optimal final measurement on the probe becomes more complicated. In such cases, mode-selective projective detection onto suitable Hermite–Gaussian modes [50, 51] provides a practical alternative, especially when parity operations and ancilla post-selection are infeasible in realistic settings.

For comparison, previous quantum metrological schemes involving indefinite causal order also exhibit a “super-Heisenberg-scaling” precision limit in estimating geometric phases [34, 35]. These schemes require a coherent superposition of different causal orders of quantum gates. In contrast, such coherent superposition is not required in our framework, a probabilistic mixture of different causal orders is sufficient to achieve the  $1/N^2$  scaling. Fundamentally, these “super-Heisenberg-scaling” enhancements originate from the noncommutativity of quantum operators in continuous-variable (CV) systems. Earlier schemes based on indefinite causal order utilize the noncommutativity of different phase-space displacements to kick a geometric phase that cannot be read out by the probe alone. By contrast, our framework utilizes the noncommutativity between free-space propagation and momentum shift, thereby kicking a dynamic phase that is accessible from the probe itself.

Moreover, we have demonstrated that the  $1/N^2$  scaling still holds when estimating a small global average parameter  $\bar{\theta}$  ( $\bar{\theta} \ll 1$ ) from the final mixed probe state alone, in which case even no classical correlation from the switch ancilla is required. (See the Supplemental Materials for details.) This result is particularly promising for a broad range of CV quantum information processing tasks, since implementing a genuine quantum switch in realistic CV platforms is highly challenging, whereas our framework only requires a probabilistic mixture of causal orders, which is significantly easier to realize experimentally.

## IV. METHODS

### A. Experimental materials

In our experiments, we used a single-frequency laser (NKT Photonics Koheras HARMONIK series) operating at a wavelength of 780 nm. The probe state is initialized as Gaussian-profile beam with a beam width of 2 mm through a collimator. A Glan–Taylor polarizer (GTP) from Thorlabs and an HWP from LBTEK are used to initialize the polarization state of light as 45°-polarized state. We set up a polarized Sagnac interferometer to implement the cyclic sensing network with a coherent superposition of opposite causal orders, where the number of sensors in the network can be scaled by adjusting the interferometer. (See the Supplemental Materials for details.) Furthermore, the unwanted relative phase induced by the interferometer is compensated through two QWPs and a HWP from LBTEK. (See the Supplemental Materials for configurations.)

To generate an angular tilt signal on each sensing node, we pasted 2 PZT chips along the horizontal plane with an interval of 20 mm on the back of a mirror. (See the Supplemental Materials for detailed design of sensor.) These PZT chips are from Core Tomorrow Company (Part No. NAC2013), they shift approximately 22 nm when a voltage of 1 V is applied. We applied two sinusoidal drive signals with opposite phases at a frequency of  $f = 10$  kHz to the two PZT chips on each signal mirror. These sinusoidal driving signals were generated by the wave generator of Moku:Pro from Liquid Instruments. We also employed a rubidium clock (Part No. STW-FS725) from Synchronization Technology to synchronize signals applied to PZT chips on different signal mirrors in our experiments.

To demodulate the average value of tilt angles, we first employed a QWP from LBTEK and a polarizer from Thorlabs to implement the weak value amplification with a fixed imaginary weak value  $A_w \approx i7$ . Subsequently, a Fourier lens and a (QPD) (Part No. 2901) from Newport were used to measure the beam position. The received optical power on the QPD was fixed around 0.2 mW in our experiments. The effective area of the QPD is  $3 \times 3$  mm<sup>2</sup>. The QPD has a responsivity of 0.5 A/W at the wavelength around 780 nm. In our experimental setup, the transresistance gain was set to 20 kV/A. Finally, the detected signal on the QPD was analyzed by the spectrum analyzer of Moku:Pro from Liquid Instruments.

### B. SNR calculation and experimental precision

In our experiments, we directly measure the differential intensity using the QPD, which converts the received optical power to an electrical voltage. According to Eq. (14), the output of QPD is a voltage signal  $V_\Delta = \gamma I_\Delta$ , where  $\gamma$  is the conversion gain, which is the product of the responsivity and transresistance gain of the QPD. Therefore, the detected signal in our experiments satisfies  $V_\Delta \propto [N^2 + (1 + 2z_{in}/\bar{z})N]\bar{\varphi}$ , which quadratically increases with the number  $N$  of sensors and linearly increases with the average tilt angle  $\bar{\varphi}$ . The loaded angular tilt signals in our experiments are synchronized sinusoidal signals at 10 kHz. To demodulate the average tilt angle, we then input the detected signal from the QPD to a spectrum analyzer. As shown in Fig. 4, we can then determine peak SNR as

$$\text{SNR} = \frac{V_\Delta^{(10 \text{ kHz})}}{V_{\text{noise}}},$$

where  $V_{\Delta}^{(10\text{ kHz})}$  corresponds to the 10 kHz signal arising from angular tilts, and  $V_{\text{noise}}$  is the noise floor in the device. Principally, the detected noise floor in the spectrum analyzer consists of shot noise, electrical noise and thermal noise, which are independent of the number of sensors and the amplitude of tilt signals. Thus, the detected peak SNR in the spectrum analyzer satisfies

$$\text{SNR} \propto \left[ N^2 + \left( 1 + 2 \frac{z_{\text{in}}}{z} \right) N \right] \bar{\varphi}^{(10\text{ kHz})}, \quad (16)$$

which also quadratically increases with the number  $N$  of sensors and linearly increases with the average tilt angle  $\bar{\varphi}$ .

In practice,  $\text{SNR} = 1$  indicates the minimum detectable signal in experiments. To determine the minimum detectable tilt angle under different number of sensors in our experiments, we conducted experiments with 1 to 9 sensors by adjusting the Sagnac interferometer. For every fixed number of sensors, we change the driving voltage on PZT chips from 1 mV to 10 mV in 1 mV increments. By measuring the corresponding SNR, we can fit the linear relation between the detected SNR and driving voltage for different number of sensors, as shown in Fig. 5. Then the minimum detectable tilt angle under different number of sensors can be inferred by taking  $\text{SNR} = 1$ . The detailed results of minimum detectable angles are listed in the Supplemental Materials.

## ACKNOWLEDGMENTS

This work was supported by the National Natural Science Foundation of China via the Excellent Young Scientists Fund (Hong Kong and Macau) Project 12322516, the National Natural Science Foundation of China (No. 62471289), Innovation Program for Quantum Science and Technology (No.2021ZD0300703), Shanghai Municipal Science and Technology Major Project (Grant No. 2019SHZDZX01), Ministry of Science and Technology, China via Quantum Science and Technology-National Science and Technology Major Project (Grant No. 2023200300600), Guangdong Provincial Quantum Science Strategic Initiative (Grant No. GDZX2503001), and the Hong Kong Research Grant Council (RGC) through grant 17303923 and grant 17302724.

**Data and Materials Availability** All data needed to evaluate the conclusions in the paper are present in the paper and the Supplementary Materials.

**Competing Interests** All authors declare that they have no competing interests.

**Author Contribution**

---

[1] C. L. Degen, F. Reinhard, and P. Cappellaro, Quantum sensing, *Rev. Mod. Phys.* **89**, 035002 (2017).

[2] J. Abadie, B. P. Abbott, R. Abbott, T. D. Abbott, M. Abernathy, C. Adams, R. Adhikari, C. Affeldt, B. Allen, G. S. Allen, E. Amador Ceron, D. Amariutei, R. S. Amin, S. B. Anderson, W. G. Anderson, K. Arai, M. A. Arain, M. C. Araya, S. M. Aston, D. Atkinson, P. Aufmuth, C. Aulbert, B. E. Aylott, S. Babak, P. Baker, S. Ballmer, D. Barker, B. Barr, P. Barriga, L. Barsotti, M. A. Barton, I. Bartos, R. Bassiri, M. Bastarrika, J. Batch, J. Bauchrowitz, B. Behnke, A. S. Bell, I. Belopolski, M. Benacquista, J. M. Berliner, A. Bertolini, J. Betzwieser, N. Beveridge, P. T. Beyersdorf, I. A. Bilenko, G. Billingsley, J. Birch, R. Biswas, E. Black, J. K. Blackburn, L. Blackburn, D. Blair, B. Bland, O. Bock, T. P. Bodiya, C. Bogan, R. Bondarescu, R. Bork, M. Born, S. Bose, P. R. Brady, V. B. Braginsky, J. E. Brau, J. Breyer, D. O. Bridges, M. Brinkmann, M. Britzger, A. F. Brooks, D. A. Brown, A. Brummitt, A. Buonanno, J. Burguet-Castell, O. Burmeister, R. L. Byer, L. Cadonati, J. B. Camp, P. Campsie, J. Cannizzo, K. Cannon, J. Cao, C. D. Capano, S. Caride, S. Caudill, M. Cavagliá, C. Cepeda, T. Chalermsongsak, E. Chalkley, P. Charlton, S. Chelkowski, Y. Chen, N. Christensen, H. Cho, S. S. Y. Chua, S. Chung, C. T. Y. Chung, G. Ciani, F. Clara, D. E. Clark, J. Clark, *et al.*, A gravitational wave observatory operating beyond the quantum shot-noise limit, *Nature Physics* **7**, 962 (2011).

[3] M. Tse, H. Yu, *et al.*, Quantum-enhanced advanced ligo detectors in the era of gravitational-wave astronomy, *Phys. Rev. Lett.* **123**, 231107 (2019).

[4] M. Abe, P. Adamson, *et al.*, Matter-wave atomic gradiometer interferometric sensor (magis-100), *Quantum Science and Technology* **6**, 044003 (2021).

[5] A. D. Ludlow, M. M. Boyd, J. Ye, E. Peik, and P. O. Schmidt, Optical atomic clocks, *Rev. Mod. Phys.* **87**, 637 (2015).

[6] K. Bongs, M. Holynski, J. Vovrosh, P. Bouyer, G. Condon, E. Rasel, C. Schubert, W. P. Schleich, and A. Roura, Taking atom interferometric quantum sensors from the laboratory to real-world applications, *Nature Reviews Physics* **1**, 731 (2019).

[7] J. S. Bennett, B. E. Vyhalek, H. Greenall, E. M. Bridge, F. Gotardo, S. Forstner, G. I. Harris, F. A. Miranda, and W. P. Bowen, Precision magnetometers for aerospace applications: A review, *Sensors* **21**, 10.3390/s21165568 (2021).

[8] W. W.-W. Hsiao, Y. Y. Hui, P.-C. Tsai, and H.-C. Chang, Fluorescent nanodiamond: A versatile tool for long-term cell tracking, super-resolution imaging, and nanoscale temperature sensing, *Accounts of Chemical Research* **49**, 400 (2016), pMID: 26882283, <https://doi.org/10.1021/acs.accounts.5b00484>.

[9] N. Aslam, H. Zhou, E. K. Urbach, M. J. Turner, R. L. Walsworth, M. D. Lukin, and H. Park, Quantum sensors for biomedical applications, *Nature Reviews Physics* **5**, 157 (2023).

[10] F. Casola, T. van der Sar, and A. Yacoby, Probing condensed matter physics with magnetometry based on nitrogen-vacancy centres in diamond, *Nature Reviews Materials* **3**, 17088 (2018).

[11] K. O. Ho, Y. Shen, Y. Y. Pang, W. K. Leung, N. Zhao, and S. Yang, Diamond quantum sensors: from physics to applications on condensed matter research, *Functional Diamond* **1**, 160 (2021), <https://doi.org/10.1080/26941112.2021.1964926>.

[12] J. Rubio, P. A. Knott, T. J. Proctor, and J. A. Dunningham, Quantum sensing networks for the estimation of linear functions, *Journal of Physics A: Mathematical and Theoretical* **53**, 344001 (2020).

[13] Z. Zhang and Q. Zhuang, Distributed quantum sensing, *Quantum Science and Technology* **6**, 043001 (2021).

[14] T. J. Proctor, P. A. Knott, and J. A. Dunningham, Multiparameter estimation in networked quantum sensors, *Phys. Rev. Lett.* **120**, 080501 (2018).

[15] Q. Zhuang, Z. Zhang, and J. H. Shapiro, Distributed quantum sensing using continuous-variable multipartite entanglement, *Phys. Rev. A* **97**, 032329 (2018).

[16] Z. Eldredge, M. Foss-Feig, J. A. Gross, S. L. Rolston, and A. V. Gorshkov, Optimal and secure measurement protocols for quantum sensor networks, *Phys. Rev. A* **97**, 042337 (2018).

[17] W. Ge, K. Jacobs, Z. Eldredge, A. V. Gorshkov, and M. Foss-Feig, Distributed quantum metrology with linear networks and separable inputs, *Phys. Rev. Lett.* **121**, 043604 (2018).

[18] M. Gessner, A. Smerzi, and L. Pezzè, Multiparameter squeezing for optimal quantum enhancements in sensor networks, *Nature Communications* **11**, 3817 (2020).

[19] L.-Z. Liu, Y.-Z. Zhang, Z.-D. Li, R. Zhang, X.-F. Yin, Y.-Y. Fei, L. Li, N.-L. Liu, F. Xu, Y.-A. Chen, and J.-W. Pan, Distributed quantum phase estimation with entangled photons, *Nature Photonics* **15**, 137 (2021).

[20] S.-R. Zhao, Y.-Z. Zhang, W.-Z. Liu, J.-Y. Guan, W. Zhang, C.-L. Li, B. Bai, M.-H. Li, Y. Liu, L. You, J. Zhang, J. Fan, F. Xu, Q. Zhang, and J.-W. Pan, Field demonstration of distributed quantum sensing without post-selection, *Phys. Rev. X* **11**, 031009 (2021).

[21] D.-H. Kim, S. Hong, Y.-S. Kim, Y. Kim, S.-W. Lee, R. C. Pooser, K. Oh, S.-Y. Lee, C. Lee, and H.-T. Lim, Distributed quantum sensing of multiple phases with fewer photons, *Nature Communications* **15**, 266 (2024).

[22] B. Liu, K.-X. Yang, Y.-L. Mao, L. Feng, B. Guo, S. Xu, H. Chen, Z.-D. Li, and J. Fan, Experimental adaptive bayesian estimation for a linear function of distributed phases in photonic quantum networks, *Optica* **11**, 1419 (2024).

[23] X. Guo, C. R. Breum, J. Borregaard, S. Izumi, M. V. Larsen, T. Gehring, M. Christandl, J. S. Neergaard-Nielsen, and U. L. Andersen, Distributed quantum sensing in a continuous-variable entangled network, *Nature Physics* **16**, 281 (2020).

[24] Y. Xia, W. Li, W. Clark, D. Hart, Q. Zhuang, and Z. Zhang, Demonstration of a reconfigurable entangled radio-frequency photonic sensor network, *Phys. Rev. Lett.* **124**, 150502 (2020).

[25] Y. Xia, A. R. Agrawal, C. M. Pluchar, A. J. Brady, Z. Liu, Q. Zhuang, D. J. Wilson, and Z. Zhang, Entanglement-enhanced optomechanical sensing, *Nature Photonics* **17**, 470 (2023).

[26] F. Flamini, N. Spagnolo, and F. Sciarrino, Photonic quantum information processing: a review, *Reports on Progress in Physics* **82**, 016001 (2018).

[27] H.-S. Zhong, Y. Li, W. Li, L.-C. Peng, Z.-E. Su, Y. Hu, Y.-M. He, X. Ding, W. Zhang, H. Li, L. Zhang, Z. Wang, L. You, X.-L. Wang, X. Jiang, L. Li, Y.-A. Chen, N.-L. Liu, C.-Y. Lu, and J.-W. Pan, 12-photon entanglement and scalable scattershot boson sampling with optimal entangled-photon pairs from parametric down-conversion, *Phys. Rev. Lett.* **121**, 250505 (2018).

[28] X. Jia, C. Zhai, X. Zhu, C. You, Y. Cao, X. Zhang, Y. Zheng, Z. Fu, J. Mao, T. Dai, L. Chang, X. Su, Q. Gong, and J. Wang, Continuous-variable multipartite entanglement in an integrated microcomb, *Nature* **639**, 329 (2025).

[29] B. M. Escher, R. L. de Matos Filho, and L. Davidovich, General framework for estimating the ultimate precision limit in noisy quantum-enhanced metrology, *Nature Physics* **7**, 406 (2011).

[30] R. Demkowicz-Dobrzański, J. Kołodyński, and M. Gută, The elusive heisenberg limit in quantum-enhanced metrology, *Nature Communications* **3**, 1063 (2012).

[31] S. Boixo, S. T. Flammia, C. M. Caves, and J. Geremia, Generalized limits for single-parameter quantum estimation, *Phys. Rev. Lett.* **98**, 090401 (2007).

[32] S. M. Roy and S. L. Braunstein, Exponentially enhanced quantum metrology, *Phys. Rev. Lett.* **100**, 220501 (2008).

[33] M. Napolitano, M. Koschorreck, B. Dubost, N. Behbood, R. J. Sewell, and M. W. Mitchell, Interaction-based quantum metrology showing scaling beyond the heisenberg limit, *Nature* **471**, 486 (2011), napolitano, M Koschorreck, M Dubost, B Behbood, N Sewell, R J Mitchell, M W eng Research Support, Non-U.S. Gov't England Nature. 2011 Mar 24;471(7339):486-9. doi: 10.1038/nature09778.

[34] X. Zhao, Y. Yang, and G. Chiribella, Quantum metrology with indefinite causal order, *Phys. Rev. Lett.* **124**, 190503 (2020).

[35] P. Yin, X. Zhao, Y. Yang, Y. Guo, W.-H. Zhang, G.-C. Li, Y.-J. Han, B.-H. Liu, J.-S. Xu, G. Chiribella, G. Chen, C.-F. Li, and G.-C. Guo, Experimental super-heisenberg quantum metrology with indefinite gate order, *Nature Physics* 10.1038/s41567-023-02046-y (2023).

[36] V. Giovannetti, S. Lloyd, and L. Maccone, Quantum metrology, *Phys. Rev. Lett.* **96**, 010401 (2006).

[37] V. Giovannetti, S. Lloyd, and L. Maccone, Advances in quantum metrology, *Nature Photonics* **5**, 222 (2011).

[38] S. L. Braunstein and P. van Loock, Quantum information with continuous variables, *Rev. Mod. Phys.* **77**, 513 (2005).

[39] C. Weedbrook, S. Pirandola, R. García-Patrón, N. J. Cerf, T. C. Ralph, J. H. Shapiro, and S. Lloyd, Gaussian quantum information, *Rev. Mod. Phys.* **84**, 621 (2012).

[40] G. Vajente, Y. Huang, M. Isi, J. C. Driggers, J. S. Kissel, M. J. Szczepańczyk, and S. Vitale, Machine-learning nonstationary

noise out of gravitational-wave detectors, *Phys. Rev. D* **101**, 042003 (2020).

[41] J.-X. Peng, B. Zhu, W. Zhang, and K. Zhang, Enhanced quantum metrology with non-phase-covariant noise, *Phys. Rev. Lett.* **133**, 090801 (2024).

[42] H. Chen, Y. Chen, J. Liu, Z. Miao, and H. Yuan, Quantum metrology enhanced by leveraging informative noise with error correction, *Phys. Rev. Lett.* **133**, 190801 (2024).

[43] N. Kong, H. Wang, M. Tian, Y. Xu, G. Chen, Y. Xiang, and Q. He, Noncommutativity as a universal characterization for enhanced quantum metrology, *Phys. Rev. Lett.* **136**, 010201 (2026).

[44] G. Chiribella, G. M. D'Ariano, P. Perinotti, and B. Valiron, Quantum computations without definite causal structure, *Phys. Rev. A* **88**, 022318 (2013).

[45] Q. Liu, Z. Hu, H. Yuan, and Y. Yang, Optimal strategies of quantum metrology with a strict hierarchy, *Phys. Rev. Lett.* **130**, 070803 (2023).

[46] K. Goswami, C. Giarmatzi, M. Kewming, F. Costa, C. Branciard, J. Romero, and A. G. White, Indefinite causal order in a quantum switch, *Phys. Rev. Lett.* **121**, 090503 (2018).

[47] P. B. Dixon, D. J. Starling, A. N. Jordan, and J. C. Howell, Ultrasensitive beam deflection measurement via interferometric weak value amplification, *Phys. Rev. Lett.* **102**, 173601 (2009).

[48] B. Xia, J. Huang, H. Li, H. Wang, and G. Zeng, Toward incompatible quantum limits on multiparameter estimation, *Nature Communications* **14**, 1021 (2023).

[49] A. N. Jordan, J. Martínez-Rincón, and J. C. Howell, Technical advantages for weak-value amplification: When less is more, *Phys. Rev. X* **4**, 011031 (2014).

[50] B. Xia, J. Huang, C. Fang, H. Li, and G. Zeng, High-precision multiparameter weak measurement with hermite-gaussian pointer, *Phys. Rev. Appl.* **13**, 034023 (2020).

[51] B. Xia, J. Huang, H. Li, M. Liu, T. Xiao, C. Fang, and G. Zeng, Ultrasensitive measurement of angular rotations via a hermite-gaussian pointer, *Photon. Res.* **10**, 2816 (2022).

# Supplementary Materials for Scaling Enhancement in Distributed Quantum Sensing via Causal Order Switching

Binke Xia,<sup>1</sup> Zhaotong Cui,<sup>2</sup> Jingzheng Huang,<sup>2,3,4,\*</sup> Yuxiang Yang,<sup>1,†</sup> and Guihua Zeng<sup>2,3,4,‡</sup>

<sup>1</sup>*QICI Quantum Information and Computation Initiative, School of Computing and Data Science, The University of Hong Kong, Pokfulam Road, Hong Kong, China*

<sup>2</sup>*State Key Laboratory of Photonics and Communications, Institute for Quantum Sensing and Information Processing, School of Automation and Intelligent Sensing, Shanghai Jiao Tong University, Shanghai 200240, China*

<sup>3</sup>*Hefei National Laboratory, Hefei 230088, China*

<sup>4</sup>*Shanghai Research Center for Quantum Sciences, Shanghai 201315, China*

---

\* [jzhuang1983@sjtu.edu.cn](mailto:jzhuang1983@sjtu.edu.cn)

† [yxyang@hku.hk](mailto:yxyang@hku.hk)

‡ [ghzeng@sjtu.edu.cn](mailto:ghzeng@sjtu.edu.cn)

## Supplementary Note 1: Quantum Precision Limits in Cyclic Sensing Network

### 1.1. Quantum Fisher information matrix

To determine the ultimate precision limits of distributed quantum sensing (DQS) schemes, we use the quantum Fisher information matrix (QFIM) as the figure of merit. The inverse of the QFIM yields the quantum Cramér–Rao bound (QCRB), a fundamental lower bound on the covariance matrix of estimating unknown parameters. Generally, we consider a parameterized quantum state  $\hat{\rho}(\mathbf{g})$ , where  $\mathbf{g} = (g_1, g_2, \dots, g_j, \dots)$  is an unknown parameter vector with  $g_j$  the  $j$ -th parameter. Then the entry of QFIM in simultaneously estimating  $g_1, g_2, \dots, g_j, \dots$  from  $\hat{\rho}(\mathbf{g})$  is given by

$$\mathcal{Q}_{jl}(\mathbf{g}) = \frac{1}{2} \text{Tr} \left( \hat{\rho}(\mathbf{g}) \{ \hat{L}_j, \hat{L}_l \} \right), \quad (\text{S1})$$

where  $\{\hat{A}, \hat{B}\} = \hat{A}\hat{B} + \hat{B}\hat{A}$  denotes the anticommutator of  $\hat{A}$  and  $\hat{B}$ , and  $\hat{L}_j(\hat{L}_l)$  is the symmetric logarithmic derivative (SLD) for the parameter  $g_j(g_l)$ , which is determined by

$$\frac{\partial \hat{\rho}(\mathbf{g})}{\partial g_j} = \frac{1}{2} \{ \hat{\rho}(\mathbf{g}), \hat{L}_j \}. \quad (\text{S2})$$

We can write the spectral decomposition of the parameterized state  $\hat{\rho}(\mathbf{g})$  as  $\hat{\rho}(\mathbf{g}) = \sum_m p_m |e_m\rangle\langle e_m|$ , where  $p_m > 0$  is the eigenvalue and  $|e_m\rangle$  is the corresponding eigenstate. Then the entry of QFIM can be calculated by

$$\mathcal{Q}_{jl}(\mathbf{g}) = \sum_m \frac{1}{p_m} \left( \frac{\partial p_m}{\partial g_j} \right) \left( \frac{\partial p_m}{\partial g_l} \right) + \sum_m 4p_m \text{Re} \left( \frac{\partial \langle e_m |}{\partial g_j} \frac{\partial |e_m \rangle}{\partial g_l} \right) - \sum_{m,n} \frac{8p_m p_n}{p_m + p_n} \text{Re} \left( \frac{\partial \langle e_m |}{\partial g_j} |e_n\rangle \langle e_n| \frac{\partial |e_m \rangle}{\partial g_l} \right). \quad (\text{S3})$$

For a pure parameterized state  $\hat{\rho}(\mathbf{g}) = |\psi(\mathbf{g})\rangle\langle\psi(\mathbf{g})|$ , Eq. (S3) can be simplified as

$$\mathcal{Q}_{jl}(\mathbf{g}) = 4 \text{Re} \left[ \frac{\partial \langle \psi(\mathbf{g}) |}{\partial g_j} \frac{\partial | \psi(\mathbf{g}) \rangle}{\partial g_l} - \frac{\partial \langle \psi(\mathbf{g}) |}{\partial g_j} |\psi(\mathbf{g})\rangle \langle \psi(\mathbf{g})| \frac{\partial | \psi(\mathbf{g}) \rangle}{\partial g_l} \right]. \quad (\text{S4})$$

Specifically, when we consider the parameters vector  $\mathbf{g}$  is encoded into a pure quantum state  $|\psi\rangle$  via a unitary evolution  $\hat{U}(\mathbf{g})$ , producing the parameterized quantum state  $|\psi(\mathbf{g})\rangle = \hat{U}(\mathbf{g})|\psi\rangle$ , then the entry of QFIM is given by

$$\mathcal{Q}_{jl}(\mathbf{g}) = 4 \text{Cov}_{|\psi\rangle} \left( \hat{\mathcal{H}}_j, \hat{\mathcal{H}}_l \right) = 2 \langle \{\hat{\mathcal{H}}_j, \hat{\mathcal{H}}_l\} \rangle - 4 \langle \hat{\mathcal{H}}_j \rangle \langle \hat{\mathcal{H}}_l \rangle \Big|_{|\psi\rangle}, \quad (\text{S5})$$

where  $\text{Cov}_{|\psi\rangle}(\hat{A}, \hat{B})$  denotes the covariance between operator  $\hat{A}$  and operator  $\hat{B}$  on quantum state  $|\psi\rangle$ , i.e.

$$\text{Cov}_{|\psi\rangle} \left( \hat{A}, \hat{B} \right) := \frac{1}{2} \langle \psi | \{\hat{A}, \hat{B}\} | \psi \rangle - \langle \psi | \hat{A} | \psi \rangle \langle \psi | \hat{B} | \psi \rangle.$$

In Eq. (S4),  $\hat{\mathcal{H}}_j$  and  $\hat{\mathcal{H}}_l$  represent the generators of parameters  $g_j$  and  $g_l$ , which can be calculated by

$$\hat{\mathcal{H}}_j = i\hat{U}^\dagger(\mathbf{g}) \left[ \frac{\partial \hat{U}(\mathbf{g})}{\partial g_j} \right]. \quad (\text{S6})$$

Generally, the QCRB is given by the inverse of QFIM. i.e.,  $\mathcal{C}_{\mathbf{g}} = [\mathcal{Q}(\mathbf{g})]^{-1}$ . In particular, when the goal is to estimate a scalar function  $f(\mathbf{g})$  of parameters  $g_1, g_2, \dots, g_j, \dots$ , the corresponding QCRB for any unbiased estimator is given by

$$\mathcal{C}_{f(\mathbf{g})} = G [\mathcal{Q}(\mathbf{g})]^{-1} G^\top, \quad (\text{S7})$$

where

$$G = \left[ \frac{\partial f(\mathbf{g})}{\partial g_1}, \frac{\partial f(\mathbf{g})}{\partial g_2}, \dots, \frac{\partial f(\mathbf{g})}{\partial g_j}, \dots \right], \quad (\text{S8})$$

denotes the associated Jacobian matrix. In principle, the QCRB  $\mathcal{C}_{f(\mathbf{g})}$  for estimating the scalar function  $f(\mathbf{g})$  is asymptotically achievable by optimal measurements in realistic experimental settings. Consequently, the variance of estimating  $f(\mathbf{g})$  satisfies

$$\text{Var}[f(\mathbf{g})] \geq \nu \mathcal{C}_{f(\mathbf{g})}, \quad (\text{S9})$$

where  $\nu$  denotes the number of independent trials. Thus, the quantum precision limit on estimating  $f(\mathbf{g})$  is denoted as

$$\delta f_{\text{QL}} = \sqrt{\nu \mathcal{C}_{f(\mathbf{g})}}. \quad (\text{S10})$$

### 1.2. Quantum precision limit for sequential query

In our scheme, we employ a cyclic sensing network, where a single probe queries  $N$  sensors sequentially. Specifically, we investigate a free-space quantum sensing scenario, where the parameter-encoding process at each sensor is described by  $\hat{U}_\theta = \exp(-i\theta\hat{X})$  and the free-space propagation between sensors is described by  $\hat{U}_z = \exp(-iz\hat{P}^2/2k)$ . By arranging  $N$  sensors inside this cyclic network in a fixed order, the evolution of the probe state throughout the sensing network can be derived as

$$\hat{U}^{(\text{Seq})} = \hat{U}_+ = \hat{U}_{z_N} \hat{U}_{\theta_N} \cdots \hat{U}_{\theta_2} \hat{U}_{z_1} \hat{U}_{\theta_1} \hat{U}_{z_0}.$$

Considering the relations

$$\begin{aligned} \hat{U}_z^\dagger \hat{X} \hat{U}_z &= \hat{X} + \frac{z}{k} \hat{P}, & \hat{U}_z^\dagger \hat{P} \hat{U}_z &= \hat{P}, \\ \hat{U}_z \hat{X} \hat{U}_z^\dagger &= \hat{X} - \frac{z}{k} \hat{P}, & \hat{U}_z \hat{P} \hat{U}_z^\dagger &= \hat{P}, \end{aligned} \quad (\text{S11})$$

and using the Baker–Campbell–Hausdorff (BCH) formula

$$e^{\hat{A}} e^{\hat{B}} = e^{\hat{A} + \hat{B} + \frac{1}{2}[\hat{A}, \hat{B}]},$$

if  $\hat{A}$  and  $\hat{B}$  commute with their commutator, i.e.,  $[\hat{A}, [\hat{A}, \hat{B}]] = [\hat{B}, [\hat{A}, \hat{B}]] = 0$ . We can then derive  $\hat{U}^{(\text{Seq})}$  as

$$\begin{aligned} \hat{U}^{(\text{Seq})} &= \exp \left[ -\frac{i}{2k} \sum_{j=0}^{N-1} z_j \left( \sum_{l=j+1}^N \theta_l \right)^2 \right] \exp \left[ -i \frac{(N+1)\bar{z}}{2k} \hat{P}^2 \right] \\ &\quad \times \exp \left[ -\frac{i}{k} \sum_{j=0}^{N-1} z_j \left( \sum_{l=j+1}^N \theta_l \right) \hat{P} \right] \exp \left[ -iN\bar{\theta}\hat{X} \right] \\ &= \exp \left[ -i \frac{(N+1)\bar{z}}{2k} \hat{P}^2 \right] \exp \left[ -\frac{i}{k} \sum_{j=0}^{N-1} z_j \left( \sum_{l=j+1}^N \theta_l \right) \hat{P} \right] \exp \left[ -iN\bar{\theta}\hat{X} \right], \end{aligned}$$

where  $\bar{\theta} = \frac{1}{N} \sum_{j=1}^N \theta_j$  denotes the average of the sensing parameters, and  $\bar{z} = \frac{1}{N+1} \sum_{j=0}^N z_j$  denotes the average propagation distance between adjacent sensors, the global phase is ignored in the final expression. For simplicity, we denote

$$g_1 = \sum_{j=0}^{N-1} z_j \left( \sum_{l=j+1}^N \theta_l \right), \quad g_2 = \sum_{j=1}^N z_j \left( \sum_{l=1}^j \theta_l \right),$$

thereby

$$g_1 + g_2 = (N+1)N\bar{z}\bar{\theta}.$$

Then the  $\hat{U}^{(\text{Seq})}$  can be denoted as

$$\hat{U}^{(\text{Seq})} = \exp \left[ -i \frac{(N+1)\bar{z}}{2k} \hat{P}^2 \right] \exp \left( -i \frac{g_1}{k} \hat{P} \right) \exp \left[ -i \frac{g_1 + g_2}{(N+1)\bar{z}} \hat{X} \right], \quad (\text{S12})$$

Substituting Eq. (S12) into Eq. (S6), we can derive the generators of parameters  $g_1$  and  $g_2$  as

$$\hat{\mathcal{H}}_1^{(\text{Seq})} = i \left[ \hat{U}^{(\text{Seq})} \right]^\dagger \left[ \frac{\partial \hat{U}^{(\text{Seq})}}{\partial g_1} \right] = \frac{\hat{X}}{(N+1)\bar{z}} + \frac{\hat{P}}{k}, \quad (\text{S13})$$

$$\hat{\mathcal{H}}_2^{(\text{Seq})} = i \left[ \hat{U}^{(\text{Seq})} \right]^\dagger \left[ \frac{\partial \hat{U}^{(\text{Seq})}}{\partial g_2} \right] = \frac{\hat{X}}{(N+1)\bar{z}}. \quad (\text{S14})$$

Then the QFIM of estimating parameters  $g_1$  and  $g_2$  is derived as

$$\mathcal{Q}^{(\text{Seq})}(g_1, g_2) = 4 \begin{pmatrix} \frac{\langle \Delta \hat{X}^2 \rangle_i}{(N+1)^2 \bar{z}^2} + \frac{\langle \Delta \hat{P}^2 \rangle_i}{k^2} + \frac{2\text{Cov}_i(\hat{X}, \hat{P})}{(N+1)\bar{z}k} & \frac{\langle \Delta \hat{X}^2 \rangle_i}{(N+1)^2 \bar{z}^2} + \frac{\text{Cov}_i(\hat{X}, \hat{P})}{(N+1)\bar{z}k} \\ \frac{\langle \Delta \hat{X}^2 \rangle_i}{(N+1)^2 \bar{z}^2} + \frac{\text{Cov}_i(\hat{X}, \hat{P})}{(N+1)\bar{z}k} & \frac{\langle \Delta \hat{X}^2 \rangle_i}{(N+1)^2 \bar{z}^2} \end{pmatrix}, \quad (\text{S15})$$

where  $\langle \Delta \hat{X}^2 \rangle_i$  and  $\langle \Delta \hat{P}^2 \rangle_i$  represent variances of position operator  $\hat{X}$  and momentum operator  $\hat{P}$  on the initial probe state  $|\psi_i\rangle$ , respectively.  $\text{Cov}_i(\hat{X}, \hat{P})$  represents the covariance between position operator  $\hat{X}$  and momentum operator  $\hat{P}$  on the initial probe state  $|\psi_i\rangle$ .

Since  $g_1 + g_2 = (N+1)N\bar{z}\theta$ , the mean  $\bar{\theta}$  of the sensing parameters  $\theta_1, \theta_2, \dots, \theta_N$  can be estimated from final parameters  $g_1$  and  $g_2$  encoded in the final probe state. The corresponding Jacobian matrix can be derived as

$$G = \left[ \frac{\partial \bar{\theta}}{\partial g_j} \right]_{j=1,2} = \left[ \frac{1}{N(N+1)\bar{z}}, \frac{1}{N(N+1)\bar{z}} \right]. \quad (\text{S16})$$

Substituting Eq. (S15) and Eq. (S16) into Eq. (S7), we can calculate the QCRB for estimating  $\bar{\theta}$  under a fixed causal order in the sensing network as

$$\mathcal{C}_{\bar{\theta}}^{(\text{Seq})} = \frac{1}{4N^2 \left[ \langle \Delta \hat{X}^2 \rangle_i - \text{Cov}_i(\hat{X}, \hat{P})^2 / \langle \Delta \hat{P}^2 \rangle_i \right]}, \quad (\text{S17})$$

which yields a Heisenberg-scaling limit

$$\delta \bar{\theta}_{\text{QL}}^{(\text{Seq})} = \sqrt{\nu \mathcal{C}_{\bar{\theta}}^{(\text{Seq})}} \propto \frac{1}{N}. \quad (\text{S18})$$

### 1.3. Quantum precision limit for quantum switch

Subsequently, we employ a quantum switch to introduce the coherent superposition of causal orders in our cyclic sensing network. Specifically, a two-level ancilla initialized in  $|\phi_{\text{SW}}\rangle = (|0\rangle + |1\rangle)/\sqrt{2}$  implements a quantum switch that controls the ordering of sensors, allowing the probe to pass through the network in a coherent superposition of two opposite causal orders. The evolution corresponding to the inverse causal order is  $\hat{U}_- = \hat{U}_{z_0} \hat{U}_{\theta_1} \hat{U}_{z_1} \hat{U}_{\theta_2} \dots \hat{U}_{\theta_N} \hat{U}_{z_N}$ . Then the joint evolution of the probe and the ancilla in the network under a superposition of opposite causal orders is given by

$$\hat{U}^{(\text{qSW})} = \hat{U}_+ \otimes |0\rangle\langle 0| + \hat{U}_- \otimes |1\rangle\langle 1|,$$

where the evolution  $\hat{U}_-$  can be calculated as

$$\begin{aligned} \hat{U}_- = & \exp \left[ -\frac{i}{2k} \sum_{j=1}^N z_j \left( \sum_{l=1}^j \theta_l \right)^2 \right] \exp \left[ -i \frac{(N+1)\bar{z}}{2k} \hat{P}^2 \right] \\ & \times \exp \left[ -\frac{i}{k} \sum_{j=1}^N z_j \left( \sum_{l=1}^j \theta_l \right) \hat{P} \right] \exp \left[ -iN\bar{\theta} \hat{X} \right]. \end{aligned}$$

Combining with the expression of  $\hat{U}_+ = \hat{U}^{(\text{Seq})}$  and substituting  $g_1$  and  $g_2$ ,  $\hat{U}^{(\text{qSW})}$  is then derived as

$$\begin{aligned} \hat{U}^{(\text{qSW})} = & \exp \left( -\frac{i}{2k} \xi_1 \right) \exp \left[ -i \frac{(N+1)\bar{z}}{2k} \hat{P}^2 \right] \exp \left( -i \frac{g_1}{k} \hat{P} \right) \exp \left[ -i \frac{g_1 + g_2}{(N+1)\bar{z}} \hat{X} \right] \otimes |0\rangle\langle 0| \\ & + \exp \left( -\frac{i}{2k} \xi_2 \right) \exp \left[ -i \frac{(N+1)\bar{z}}{2k} \hat{P}^2 \right] \exp \left( -i \frac{g_2}{k} \hat{P} \right) \exp \left[ -i \frac{g_1 + g_2}{(N+1)\bar{z}} \hat{X} \right] \otimes |1\rangle\langle 1|, \end{aligned}$$

where

$$\xi_1 = \sum_{j=0}^{N-1} z_j \left( \sum_{l=j+1}^N \theta_l \right)^2, \quad \xi_2 = \sum_{j=1}^N z_j \left( \sum_{l=1}^j \theta_l \right)^2.$$

Furthermore, we note that

$$\begin{aligned}
\xi_1 - \xi_2 &= (z_0 - z_N) \left( \sum_{l=1}^N \theta_l \right)^2 + \sum_{j=1}^{N-1} z_j \left[ \left( \sum_{l=j+1}^N \theta_l \right)^2 - \left( \sum_{l=1}^j \theta_l \right)^2 \right] \\
&= (z_0 - z_N) \left( \sum_{l=1}^N \theta_l \right)^2 + \left[ \sum_{j=1}^{N-1} z_j \left( \sum_{l=j+1}^N \theta_l - \sum_{l=1}^j \theta_l \right) \right] \cdot \sum_{l=1}^N \theta_l \\
&= \left[ \sum_{j=0}^{N-1} z_j \left( \sum_{l=j+1}^N \theta_l \right) - \sum_{j=1}^N z_j \left( \sum_{l=1}^j \theta_l \right) \right] \cdot \sum_{l=1}^N \theta_l \\
&= (g_1 - g_2) \cdot N \bar{\theta} = \frac{g_1^2 - g_2^2}{(N+1)\bar{z}}.
\end{aligned}$$

Ignoring a global phase of  $-(\xi_1 + \xi_2)/4k$ , the joint evolution  $\hat{U}^{(\text{qSW})}$  is finally given by

$$\begin{aligned}
\hat{U}^{(\text{qSW})} &= \exp \left[ -i \frac{g_1^2 - g_2^2}{4k(N+1)\bar{z}} \right] \exp \left[ -i \frac{(N+1)\bar{z}}{2k} \hat{P}^2 \right] \exp \left( -i \frac{g_1}{k} \hat{P} \right) \exp \left[ -i \frac{g_1 + g_2}{(N+1)\bar{z}} \hat{X} \right] \otimes |0\rangle\langle 0| \\
&\quad + \exp \left[ i \frac{g_1^2 - g_2^2}{4k(N+1)\bar{z}} \right] \exp \left[ -i \frac{(N+1)\bar{z}}{2k} \hat{P}^2 \right] \exp \left( -i \frac{g_2}{k} \hat{P} \right) \exp \left[ -i \frac{g_1 + g_2}{(N+1)\bar{z}} \hat{X} \right] \otimes |1\rangle\langle 1|.
\end{aligned} \quad (\text{S19})$$

Substituting Eq. (S19) into Eq. (S6), we can derive the generators of parameters  $g_1$  and  $g_2$  as

$$\hat{\mathcal{H}}_1^{(\text{qSW})} = i \left[ \hat{U}^{(\text{qSW})} \right]^\dagger \left[ \frac{\partial \hat{U}^{(\text{qSW})}}{\partial g_1} \right] = \frac{\hat{X}}{(N+1)\bar{z}} \otimes \hat{\mathbb{I}} + \left[ \frac{\hat{P}}{k} - \frac{g_2}{k(N+1)\bar{z}} \right] \otimes |0\rangle\langle 0|, \quad (\text{S20})$$

$$\hat{\mathcal{H}}_2^{(\text{qSW})} = i \left[ \hat{U}^{(\text{qSW})} \right]^\dagger \left[ \frac{\partial \hat{U}^{(\text{qSW})}}{\partial g_2} \right] = \frac{\hat{X}}{(N+1)\bar{z}} \otimes \hat{\mathbb{I}} + \left[ \frac{\hat{P}}{k} - \frac{g_1}{k(N+1)\bar{z}} \right] \otimes |1\rangle\langle 1|. \quad (\text{S21})$$

The joint initial state of the probe and the ancilla is denoted as  $|\Psi_i\rangle = |\psi_i\rangle \otimes |\phi_{\text{SW}}\rangle$ , where  $|\phi_{\text{SW}}\rangle = (|0\rangle + |1\rangle)/\sqrt{2}$ . Then we can calculate that

$$\begin{aligned}
\text{Var}_{|\Psi_i\rangle} \left[ \hat{\mathcal{H}}_1^{(\text{qSW})} \right] &= \frac{\langle \Delta \hat{X}^2 \rangle_i}{(N+1)^2 \bar{z}^2} + \frac{\langle \Delta \hat{P}^2 \rangle_i}{2k^2} + \left[ \frac{\langle \hat{P} \rangle_i}{2k} - \frac{g_2}{2k(N+1)\bar{z}} \right]^2 + \frac{\text{Cov}_i(\hat{X}, \hat{P})}{(N+1)\bar{z}k}, \\
\text{Cov}_{|\Psi_i\rangle} \left[ \hat{\mathcal{H}}_1^{(\text{qSW})}, \hat{\mathcal{H}}_2^{(\text{qSW})} \right] &= \frac{\langle \Delta \hat{X}^2 \rangle_i}{(N+1)^2 \bar{z}^2} - \left[ \frac{\langle \hat{P} \rangle_i}{2k} - \frac{g_2}{2k(N+1)\bar{z}} \right] \cdot \left[ \frac{\langle \hat{P} \rangle_i}{2k} - \frac{g_1}{2k(N+1)\bar{z}} \right] + \frac{\text{Cov}_i(\hat{X}, \hat{P})}{(N+1)\bar{z}k}, \\
\text{Cov}_{|\Psi_i\rangle} \left[ \hat{\mathcal{H}}_2^{(\text{qSW})}, \hat{\mathcal{H}}_1^{(\text{qSW})} \right] &= \text{Cov}_{|\Psi_i\rangle} \left[ \hat{\mathcal{H}}_1^{(\text{qSW})}, \hat{\mathcal{H}}_2^{(\text{qSW})} \right], \\
\text{Var}_{|\Psi_i\rangle} \left[ \hat{\mathcal{H}}_2^{(\text{qSW})} \right] &= \frac{\langle \Delta \hat{X}^2 \rangle_i}{(N+1)^2 \bar{z}^2} + \frac{\langle \Delta \hat{P}^2 \rangle_i}{2k^2} + \left[ \frac{\langle \hat{P} \rangle_i}{2k} - \frac{g_1}{2k(N+1)\bar{z}} \right]^2 + \frac{\text{Cov}_i(\hat{X}, \hat{P})}{(N+1)\bar{z}k},
\end{aligned} \quad (\text{S22})$$

where  $\langle \Delta \hat{X}^2 \rangle_i$  and  $\langle \Delta \hat{P}^2 \rangle_i$  represent variances of position operator  $\hat{X}$  and momentum operator  $\hat{P}$  on the initial probe state  $|\psi_i\rangle$ , respectively.  $\langle \hat{P} \rangle_i$  represents the initial mean momentum of the probe state  $|\psi_i\rangle$ , and  $\text{Cov}_i(\hat{X}, \hat{P})$  represents the covariance between position operator  $\hat{X}$  and momentum operator  $\hat{P}$  on the initial probe state  $|\psi_i\rangle$ . Then the QFIM of estimating parameters  $g_1$  and  $g_2$  is given by

$$\mathcal{Q}^{(\text{qSW})}(g_1, g_2) = 4 \left\{ \begin{array}{c} \text{Var}_{|\Psi_i\rangle} \left[ \hat{\mathcal{H}}_1^{(\text{qSW})} \right] \quad \text{Cov}_{|\Psi_i\rangle} \left[ \hat{\mathcal{H}}_1^{(\text{qSW})}, \hat{\mathcal{H}}_2^{(\text{qSW})} \right] \\ \text{Cov}_{|\Psi_i\rangle} \left[ \hat{\mathcal{H}}_2^{(\text{qSW})}, \hat{\mathcal{H}}_1^{(\text{qSW})} \right] \quad \text{Var}_{|\Psi_i\rangle} \left[ \hat{\mathcal{H}}_2^{(\text{qSW})} \right] \end{array} \right\}, \quad (\text{S23})$$

Combining with the Jacobian matrix in Eq. (S16), and substituting them into Eq. (S7), we can calculate the QCRB for estimating  $\bar{\theta}$  under an indefinite causal order in the sensing network as

$$\mathcal{C}_{\bar{\theta}}^{(\text{qSW})} = \frac{1}{4N^2(N+1)^2 \bar{z}^2} \frac{\text{Var}_{|\Psi_i\rangle} \left[ \hat{\mathcal{H}}_1^{(\text{qSW})} \right] + \text{Var}_{|\Psi_i\rangle} \left[ \hat{\mathcal{H}}_2^{(\text{qSW})} \right] - 2\text{Cov}_{|\Psi_i\rangle} \left[ \hat{\mathcal{H}}_1^{(\text{qSW})}, \hat{\mathcal{H}}_2^{(\text{qSW})} \right]}{\text{Var}_{|\Psi_i\rangle} \left[ \hat{\mathcal{H}}_1^{(\text{qSW})} \right] \cdot \text{Var}_{|\Psi_i\rangle} \left[ \hat{\mathcal{H}}_2^{(\text{qSW})} \right] - \text{Cov}_{|\Psi_i\rangle} \left[ \hat{\mathcal{H}}_1^{(\text{qSW})}, \hat{\mathcal{H}}_2^{(\text{qSW})} \right]^2}. \quad (\text{S24})$$

Combining with Eq. (S22), we can determine that

$$\begin{aligned} & \lim_{N \rightarrow \infty} \frac{\text{Var}_{|\Psi_i\rangle} [\hat{\mathcal{H}}_1^{(\text{qSW})}] + \text{Var}_{|\Psi_i\rangle} [\hat{\mathcal{H}}_2^{(\text{qSW})}] - 2\text{Cov}_{|\Psi_i\rangle} [\hat{\mathcal{H}}_1^{(\text{qSW})}, \hat{\mathcal{H}}_2^{(\text{qSW})}]}{\text{Var}_{|\Psi_i\rangle} [\hat{\mathcal{H}}_1^{(\text{qSW})}] \cdot \text{Var}_{|\Psi_i\rangle} [\hat{\mathcal{H}}_2^{(\text{qSW})}] - \text{Cov}_{|\Psi_i\rangle} [\hat{\mathcal{H}}_1^{(\text{qSW})}, \hat{\mathcal{H}}_2^{(\text{qSW})}]^2} \\ &= \frac{\langle \Delta \hat{P}^2 \rangle_i / k^2 + \langle \hat{P} \rangle_i^2 / k^2}{\left( \langle \Delta \hat{P}^2 \rangle_i / 2k^2 + \langle \hat{P} \rangle_i^2 / 4k^2 \right)^2 - \left( \langle \hat{P} \rangle_i^2 / 4k^2 \right)^2} \\ &= \frac{4k^2}{\langle \Delta \hat{P}^2 \rangle_i}. \end{aligned}$$

Thus, we can further determine that

$$\lim_{N \rightarrow \infty} \mathcal{C}_{\bar{\theta}}^{(\text{qSW})} / N^{-4} = \frac{k^2}{\bar{z}^2 \Delta \hat{P}^2}, \quad (\text{S25})$$

which yields a “super-Heisenberg-scaling” limit

$$\lim_{N \rightarrow \infty} \delta \bar{\theta}_{\text{QL}}^{(\text{qSW})} / N^{-2} = \lim_{N \rightarrow \infty} \sqrt{\nu \mathcal{C}_{\bar{\theta}}^{(\text{qSW})}} / N^{-2} = \text{const.} \quad (\text{S26})$$

#### 1.4. Quantum precision limit for classical switch

According to Eq. (S22) to Eq. (S25), we can see that the relative phase of ancilla does not contribute to the  $N^{-4}$ -scaling enhancement in the QCRB, and the  $N^4$  terms are totally encoded into the probe’s displacement. This result indicates that it is not necessary to employ a quantum switch in this cyclic sensing network, a probabilistic mixture of opposite causal orders introduced by a classical switch is capable of achieving the  $N^{-4}$ -scaling enhancement. Therefore, we employ a classically mixed state  $\hat{\rho}_{\text{SW}} = (|0\rangle\langle 0| + |1\rangle\langle 1|)/2$  to probabilistically switch the causal order of probe state in the cyclic network. In this case, the probe passes through the cyclic network in either the forward or reverse direction with equal probability. Then the final joint state of the probe and the ancilla can be derived as

$$\hat{\rho}_f^{(\text{cSW})} = \frac{1}{2} \hat{U}_+ |\psi_i\rangle\langle\psi_i| \hat{U}_+^\dagger \otimes |0\rangle\langle 0| + \frac{1}{2} \hat{U}_- |\psi_i\rangle\langle\psi_i| \hat{U}_-^\dagger \otimes |1\rangle\langle 1|, \quad (\text{S27})$$

where  $\hat{U}_+$  and  $\hat{U}_-$  are the evolution operators of forward and backward propagations given by

$$\begin{aligned} \hat{U}_+ &= \hat{U}_{z_N} \hat{U}_{\theta_N} \cdots \hat{U}_{\theta_2} \hat{U}_{z_1} \hat{U}_{\theta_1} \hat{U}_{z_0} = \exp \left[ -i \frac{(N+1)\bar{z}}{2k} \hat{P}^2 \right] \exp \left( -i \frac{g_1}{k} \hat{P} \right) \exp \left[ -i \frac{g_1+g_2}{(N+1)\bar{z}} \hat{X} \right], \\ \hat{U}_- &= \hat{U}_{z_0} \hat{U}_{\theta_1} \hat{U}_{z_1} \hat{U}_{\theta_2} \cdots \hat{U}_{\theta_N} \hat{U}_{z_N} = \exp \left[ -i \frac{(N+1)\bar{z}}{2k} \hat{P}^2 \right] \exp \left( -i \frac{g_2}{k} \hat{P} \right) \exp \left[ -i \frac{g_1+g_2}{(N+1)\bar{z}} \hat{X} \right]. \end{aligned}$$

Here the switch ancilla serves as a classical label that encodes classical correlations, enabling one to distinguish the direction of the probe state in the network. In contrast to the case of a quantum switch, the final joint state obtained with a classical switch is a mixed state, so the corresponding QFIM cannot be calculated using generator-based formulas. However, the final state  $\hat{\rho}_f^{(\text{cSW})}$  admits as a spectral decomposition with eigenvalues  $p_+ = p_- = 1/2$  and corresponding eigenstates  $|\Psi_+\rangle = |\psi_+\rangle \otimes |0\rangle$  and  $|\Psi_-\rangle = |\psi_-\rangle \otimes |0\rangle$ , where  $|\psi_+\rangle = \hat{U}_+ |\psi_i\rangle$  and  $|\psi_-\rangle = \hat{U}_- |\psi_i\rangle$ . Substituting it into Eq. (S3), we can calculate that the entry of QFIM for simultaneously estimating  $g_1$  and  $g_2$  from  $\hat{\rho}_f^{(\text{cSW})}$  is given by

$$\begin{aligned} \mathcal{Q}_{jl}^{(\text{cSW})}(g_1, g_2) &= 2\text{Re} \left( \frac{\partial \langle \psi_+ |}{\partial g_j} \frac{\partial | \psi_+ \rangle}{\partial g_l} \right) - 2\text{Re} \left( \frac{\partial \langle \psi_+ |}{\partial g_j} | \psi_+ \rangle \langle \psi_+ | \frac{\partial | \psi_+ \rangle}{\partial g_l} \right) \\ &\quad + 2\text{Re} \left( \frac{\partial \langle \psi_- |}{\partial g_j} \frac{\partial | \psi_- \rangle}{\partial g_l} \right) - 2\text{Re} \left( \frac{\partial \langle \psi_- |}{\partial g_j} | \psi_- \rangle \langle \psi_- | \frac{\partial | \psi_- \rangle}{\partial g_l} \right), \end{aligned}$$

for  $j, l = 1, 2$ , because  $p_+ = p_- = 1/2$  are independent of parameters and  $\partial_{g_j} |\Psi_+\rangle$  is orthogonal to  $|\Psi_-\rangle$  while  $\partial_{g_j} |\Psi_-\rangle$  is orthogonal to  $|\Psi_+\rangle$ . According to Eq. (S4), the QFIM  $\mathcal{Q}^{(\text{cSW})}(g_1, g_2)$  can be calculated by

$$\mathcal{Q}^{(\text{cSW})}(g_1, g_2) = \frac{1}{2} \mathcal{Q}(g_1, g_2 || |\psi_+\rangle) + \frac{1}{2} \mathcal{Q}(g_1, g_2 || |\psi_-\rangle),$$

where  $\mathcal{Q}(g_1, g_2 || \psi_+ \rangle)$  and  $\mathcal{Q}(g_1, g_2 || \psi_- \rangle)$  are the QFIMs of two pure states  $|\psi_+\rangle$  and  $|\psi_-\rangle$ , respectively. Drawing on the calculations of  $\mathcal{Q}^{(\text{Seq})}(g_1, g_2)$ , we can separately calculate the QFIMs of estimating  $g_1$  and  $g_2$  from  $|\psi_+\rangle$  and  $|\psi_-\rangle$  as

$$\begin{aligned}\mathcal{Q}(g_1, g_2 || \psi_+ \rangle) &= \mathcal{Q}^{(\text{Seq}, +)}(g_1, g_2) = 4 \begin{pmatrix} \frac{\langle \Delta \hat{X}^2 \rangle_i}{(N+1)^2 \bar{z}^2} + \frac{\langle \Delta \hat{P}^2 \rangle_i}{k^2} + \frac{2\text{Cov}_i(\hat{X}, \hat{P})}{(N+1)\bar{z}k} & \frac{\langle \Delta \hat{X}^2 \rangle_i}{(N+1)^2 \bar{z}^2} + \frac{\text{Cov}_i(\hat{X}, \hat{P})}{(N+1)\bar{z}k} \\ \frac{\langle \Delta \hat{X}^2 \rangle_i}{(N+1)^2 \bar{z}^2} + \frac{\text{Cov}_i(\hat{X}, \hat{P})}{(N+1)\bar{z}k} & \frac{\langle \Delta \hat{X}^2 \rangle_i}{(N+1)^2 \bar{z}^2} \end{pmatrix}, \\ \mathcal{Q}(g_1, g_2 || \psi_- \rangle) &= \mathcal{Q}^{(\text{Seq}, -)}(g_1, g_2) = 4 \begin{pmatrix} \frac{\langle \Delta \hat{X}^2 \rangle_i}{(N+1)^2 \bar{z}^2} & \frac{\langle \Delta \hat{X}^2 \rangle_i}{(N+1)^2 \bar{z}^2} + \frac{\text{Cov}_i(\hat{X}, \hat{P})}{(N+1)\bar{z}k} \\ \frac{\langle \Delta \hat{X}^2 \rangle_i}{(N+1)^2 \bar{z}^2} + \frac{\text{Cov}_i(\hat{X}, \hat{P})}{(N+1)\bar{z}k} & \frac{\langle \Delta \hat{X}^2 \rangle_i}{(N+1)^2 \bar{z}^2} + \frac{\langle \Delta \hat{P}^2 \rangle_i}{k^2} + \frac{2\text{Cov}_i(\hat{X}, \hat{P})}{(N+1)\bar{z}k} \end{pmatrix}.\end{aligned}$$

Finally, the QFIM of estimating  $g_1$  and  $g_2$  using a classical switch is given as

$$\mathcal{Q}^{(\text{cSW})}(g_1, g_2) = 4 \begin{pmatrix} \frac{\langle \Delta \hat{X}^2 \rangle_i}{(N+1)^2 \bar{z}^2} + \frac{\langle \Delta \hat{P}^2 \rangle_i}{2k^2} + \frac{\text{Cov}_i(\hat{X}, \hat{P})}{(N+1)\bar{z}k} & \frac{\langle \Delta \hat{X}^2 \rangle_i}{(N+1)^2 \bar{z}^2} + \frac{\text{Cov}_i(\hat{X}, \hat{P})}{(N+1)\bar{z}k} \\ \frac{\langle \Delta \hat{X}^2 \rangle_i}{(N+1)^2 \bar{z}^2} + \frac{\text{Cov}_i(\hat{X}, \hat{P})}{(N+1)\bar{z}k} & \frac{\langle \Delta \hat{X}^2 \rangle_i}{(N+1)^2 \bar{z}^2} + \frac{\langle \Delta \hat{P}^2 \rangle_i}{2k^2} + \frac{\text{Cov}_i(\hat{X}, \hat{P})}{(N+1)\bar{z}k} \end{pmatrix}. \quad (\text{S28})$$

Combining with the Jacobian matrix in Eq. (S16), and substituting them into Eq. (S7), the QCRB for estimating  $\bar{\theta}$  with a mixing strategy of opposite causal orders in the sensing network satisfies

$$\mathcal{C}_{\bar{\theta}}^{(\text{cSW})} = \frac{k^2}{N^2(N+1)^2 \bar{z}^2 \langle \Delta \hat{P}^2 \rangle_i + 4N^2(N+1)\bar{z}k \text{Cov}_i(\hat{X}, \hat{P})^2 + 4N^2k^2 \langle \Delta \hat{X}^2 \rangle_i}, \quad (\text{S29})$$

which indicates that

$$\lim_{N \rightarrow \infty} \mathcal{C}_{\bar{\theta}}^{(\text{cSW})}/N^{-4} = \frac{k^2}{\bar{z}^2 \Delta \hat{P}^2}. \quad (\text{S30})$$

Therefore, the classical switch yields the same scaling in quantum precision limit with the quantum switch in our scheme

$$\lim_{N \rightarrow \infty} \delta \bar{\theta}_{\text{QL}}^{(\text{cSW})}/N^{-2} = \lim_{N \rightarrow \infty} \sqrt{\nu \mathcal{C}_{\bar{\theta}}^{(\text{cSW})}}/N^{-2} = \text{const.} \quad (\text{S31})$$

### 1.5. Estimation of $\bar{\theta}$ from mixed final probe state alone

By using either a quantum or a classical switch, the global parameter is estimated from the final joint state of the probe and ancilla. Here, we further investigate the estimation of the global parameter  $\bar{\theta}$  from the mixed probe state alone. In this case, the final probe state can be obtained by tracing out the ancilla

$$\hat{\rho}_f^{(\text{P})} = \text{Tr}_{\text{ancilla}} \left[ \hat{\rho}_f^{(\text{cSW})} \right] = \frac{1}{2} |\psi_+\rangle \langle \psi_+| + \frac{1}{2} |\psi_-\rangle \langle \psi_-|, \quad (\text{S32})$$

which is a probability mixing of two pure state  $|\psi_+\rangle$  and  $|\psi_-\rangle$ . Due to the convexity of QFIM, the QFIM of estimating  $g_1$  and  $g_2$  from  $\hat{\rho}_f^{(\text{P})}$  satisfies

$$\mathcal{Q}(g_1, g_2 | \hat{\rho}_f^{(\text{P})}) \leq \frac{1}{2} \mathcal{Q}(g_1, g_2 || \psi_+ \rangle) + \frac{1}{2} \mathcal{Q}(g_1, g_2 || \psi_- \rangle) = \mathcal{Q}^{(\text{cSW})}(g_1, g_2). \quad (\text{S33})$$

Although it is intractable to determine whether the above bound is always attainable, we can show that the  $N^{-4}$ -scaling enhancement in QCRB is attainable in the regime of small parameters, i.e., for  $g_1 \ll 1$  and  $g_2 \ll 1$ . In this case, it is equivalent to calculate the QFIM at  $\mathbf{g} = \mathbf{0}$ . Here we denote

$$\hat{U}_{\bar{z}} = \exp \left[ -i \frac{(N+1)\bar{z}}{2k} \hat{P}^2 \right], \quad \hat{V}_+ = \exp \left( -i \frac{g_1}{k} \hat{P} \right) \exp \left[ -i \frac{g_1 + g_2}{(N+1)\bar{z}} \hat{X} \right], \quad \hat{V}_- = \exp \left( -i \frac{g_2}{k} \hat{P} \right) \exp \left[ -i \frac{g_1 + g_2}{(N+1)\bar{z}} \hat{X} \right],$$

then we have

$$\hat{U}_+ = \hat{U}_{\bar{z}} \hat{V}_+, \quad \hat{U}_- = \hat{U}_{\bar{z}} \hat{V}_-.$$

The final probe state at  $\mathbf{g} = \mathbf{0}$  can be written as

$$\hat{\rho}_f^{(P)} \Big|_{\mathbf{g}=\mathbf{0}} = \hat{U}_{\bar{z}} |\psi_i\rangle\langle\psi_i| \hat{U}_{\bar{z}}^\dagger, \quad (\text{S34})$$

which is a pure state. However, variations of parameters at  $\mathbf{g} = \mathbf{0}$  still drive the final probe state into a mixed state. Therefore, we must directly apply Eq. (S1) to calculate the QFIM of  $g_1$  and  $g_2$  from  $\hat{\rho}_f^{(P)}$  at  $\mathbf{g} = \mathbf{0}$ . Therefore, we first calculate the derivatives of  $\hat{\rho}_f^{(P)}$  with respect  $g_1$  and  $g_2$  at  $\mathbf{g} = \mathbf{0}$ , which can be obtained from

$$\begin{aligned} \frac{\partial \hat{U}_+}{\partial g_1} \Big|_{\mathbf{g}=\mathbf{0}} &= \hat{U}_{\bar{z}} \frac{\partial \hat{V}_+}{\partial g_1} \Big|_{\mathbf{g}=\mathbf{0}} = -i\hat{U}_{\bar{z}} \hat{H}_1, & \frac{\partial \hat{U}_+}{\partial g_2} \Big|_{\mathbf{g}=\mathbf{0}} &= \hat{U}_{\bar{z}} \frac{\partial \hat{V}_+}{\partial g_2} \Big|_{\mathbf{g}=\mathbf{0}} = -i\hat{U}_{\bar{z}} \hat{H}_2, \\ \frac{\partial \hat{U}_-}{\partial g_1} \Big|_{\mathbf{g}=\mathbf{0}} &= \hat{U}_{\bar{z}} \frac{\partial \hat{V}_-}{\partial g_1} \Big|_{\mathbf{g}=\mathbf{0}} = -i\hat{U}_{\bar{z}} \hat{H}_2, & \frac{\partial \hat{U}_-}{\partial g_2} \Big|_{\mathbf{g}=\mathbf{0}} &= \hat{U}_{\bar{z}} \frac{\partial \hat{V}_-}{\partial g_2} \Big|_{\mathbf{g}=\mathbf{0}} = -i\hat{U}_{\bar{z}} \hat{H}_1, \end{aligned}$$

where

$$\hat{H}_1 = \frac{\hat{P}}{k} + \frac{\hat{X}}{(N+1)\bar{z}}, \quad \hat{H}_2 = \frac{\hat{X}}{(N+1)\bar{z}},$$

which are Hermitian operators. Then the derivatives of  $\hat{\rho}_f^{(P)}$  is given by

$$\begin{aligned} \frac{\partial \hat{\rho}_f^{(P)}}{\partial g_1} \Big|_{\mathbf{g}=\mathbf{0}} &= -\frac{i}{2} \hat{U}_{\bar{z}} \hat{H}_1 |\psi_i\rangle\langle\psi_i| \hat{U}_{\bar{z}}^\dagger + \frac{i}{2} \hat{U}_{\bar{z}} |\psi_i\rangle\langle\psi_i| \hat{H}_1 \hat{U}_{\bar{z}}^\dagger - \frac{i}{2} \hat{U}_{\bar{z}} \hat{H}_2 |\psi_i\rangle\langle\psi_i| \hat{U}_{\bar{z}}^\dagger + \frac{i}{2} \hat{U}_{\bar{z}} |\psi_i\rangle\langle\psi_i| \hat{H}_2 \hat{U}_{\bar{z}}^\dagger, \\ \frac{\partial \hat{\rho}_f^{(P)}}{\partial g_2} \Big|_{\mathbf{g}=\mathbf{0}} &= -\frac{i}{2} \hat{U}_{\bar{z}} \hat{H}_2 |\psi_i\rangle\langle\psi_i| \hat{U}_{\bar{z}}^\dagger + \frac{i}{2} \hat{U}_{\bar{z}} |\psi_i\rangle\langle\psi_i| \hat{H}_2 \hat{U}_{\bar{z}}^\dagger - \frac{i}{2} \hat{U}_{\bar{z}} \hat{H}_1 |\psi_i\rangle\langle\psi_i| \hat{U}_{\bar{z}}^\dagger + \frac{i}{2} \hat{U}_{\bar{z}} |\psi_i\rangle\langle\psi_i| \hat{H}_1 \hat{U}_{\bar{z}}^\dagger, \end{aligned}$$

which can be further derived as

$$\frac{\partial \hat{\rho}_f^{(P)}}{\partial g_1} \Big|_{\mathbf{g}=\mathbf{0}} = \frac{\partial \hat{\rho}_f^{(P)}}{\partial g_2} \Big|_{\mathbf{g}=\mathbf{0}} = -\frac{i}{2} \hat{U}_{\bar{z}} [\hat{H}_1 + \hat{H}_2, |\psi_i\rangle\langle\psi_i|] \hat{U}_{\bar{z}}^\dagger. \quad (\text{S35})$$

Here we denote

$$\hat{H}_0 = \hat{H}_1 + \hat{H}_2 = \frac{\hat{P}}{k} + \frac{2\hat{X}}{(N+1)\bar{z}},$$

and substitute Eq. (S34) and Eq. (S35) into Eq. (S2), the SLD operators of parameters  $g_1$  and  $g_2$  is given by

$$\hat{L}_1 \Big|_{\mathbf{g}=\mathbf{0}} = \hat{L}_2 \Big|_{\mathbf{g}=\mathbf{0}} = -i\hat{U}_{\bar{z}} [\hat{H}_0, |\psi_i\rangle\langle\psi_i|] \hat{U}_{\bar{z}}^\dagger. \quad (\text{S36})$$

Substituting Eq. (S34) and Eq. (S36) into Eq. (S1), we can calculate the corresponding QFIM at  $\mathbf{g} = \mathbf{0}$  as

$$\mathcal{Q}(g_1, g_2 | \hat{\rho}_f^{(P)}) \Big|_{\mathbf{g}=\mathbf{0}} = \text{Var}_{|\psi_i\rangle}(\hat{H}_0) \begin{pmatrix} 1 & 1 \\ 1 & 1 \end{pmatrix},$$

which is a singular matrix. However, this singular QFIM can be diagonalized as  $\text{Var}_{|\psi_i\rangle}(\hat{H}_0)\text{diag}(2, 0)$ , where the nonzero eigenvalue  $2\text{Var}_{|\psi_i\rangle}(\hat{H}_0)$  corresponds to the eigenvector  $(1/\sqrt{2}, 1/\sqrt{2})^\top$ . This result indicates that only the parameter summation  $g_1 + g_2$  is estimable, whose QFI is given by

$$\mathcal{Q}(g_1 + g_2 | \hat{\rho}_f^{(P)}) \Big|_{\mathbf{g}=\mathbf{0}} = \text{Var}_{|\psi_i\rangle}(\hat{H}_0) = \frac{1}{N^2(N+1)^2\bar{z}^2} \mathcal{Q}(\bar{\theta} | \hat{\rho}_f^{(P)}) \Big|_{\mathbf{g}=\mathbf{0}}.$$

Then the corresponding QCRB on estimating global parameter  $\bar{\theta}$  at  $\mathbf{g} = \mathbf{0}$  is given by

$$\mathcal{C}_{\bar{\theta}}^{(P)} \Big|_{\mathbf{g}=\mathbf{0}} = \frac{1}{N^2(N+1)^2\bar{z}^2 \text{Var}_{|\psi_i\rangle}(\hat{H}_0)} = \mathcal{C}_{\bar{\theta}}^{(\text{cSW})}. \quad (\text{S37})$$

According to Eq. (S30) and Eq. (S31), we conclude that estimating  $\bar{\theta}$  from the mixed final probe alone can also achieve a "super-Heisenberg-scaling" limit in the small-parameter regime.

## Supplementary Note 2: Experimental Configurations

In this section, we supplement the configuration details in our experiments, specifically scaling the network size by adjusting the Sagnac interferometer and compensating the unwanted relative phase introduced in the interferometer using wave plates.

## 2.1. Configuration of sensing network

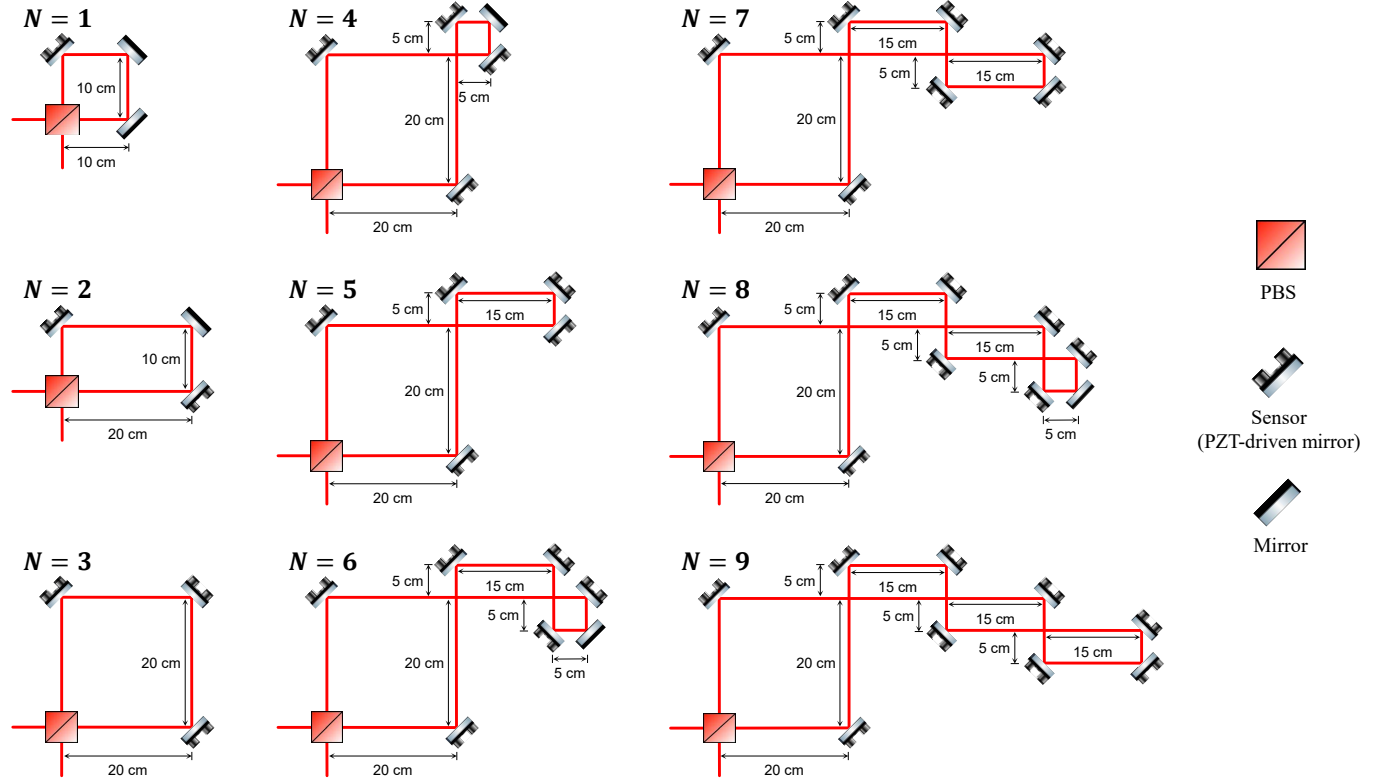


Figure S1. Configuration of sensing network with different number of sensors.

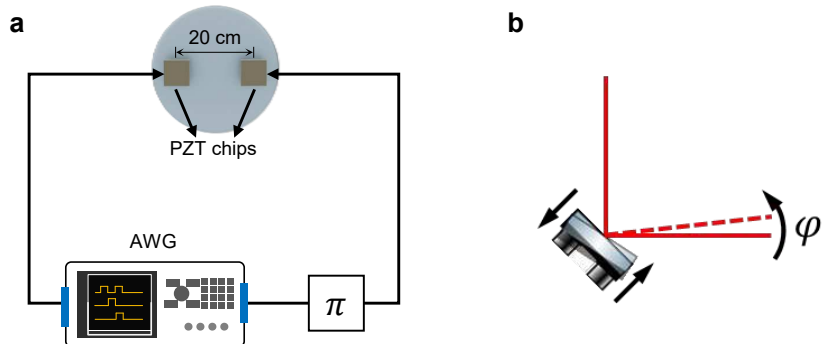


Figure S2. Design of sensing node. **a** Configuration and applied signals of PZT chips. **b** Tilt generation.

In our experiments, we scale the size of the sensing network by reconfiguring the Sagnac interferometer, as shown in Figure S1. To ensure effective weak value amplification, the interferometer is configured with an odd number of mirrors. Accordingly, mirrors driven by PZT chips serve as sensors, whereas mirrors without PZT actuation are used solely to complete the interferometric path. In Figure S1, we illustrate the interferometer setup for sensing networks

comprising 1 sensor to 9 sensors. The total interferometer length is configured as  $(N + 1) \times 20$  cm, where  $N$  denotes the number of sensors and  $\bar{z} = 20$  cm is the average propagation distance between two adjacent nodes. Additionally, the sensing node is realized using a mirror actuated by two PZT chips in our experiments, and its design is presented in Figure S2. Two PZT chips are pasted on the back surface of a mirror along the horizontal plane with an interval of 20 mm. These PZT chips shift approximately 22 nm when a voltage of 1 V is applied. As shown in Figure S2a, we apply two sinusoidal signals with opposite phases to the two PZT chips. Thus, a 1 V peak-to-peak drive signal corresponds to a 1.1  $\mu$ rad tilt angle on the mirror, which leads to a 2.2  $\mu$ rad beam-tilt modulation.

## 2.2. Compensation for relative phase

In practice, experimental imperfections, such as interferometer misalignment and polarization-dependent mirror reflectivities, can introduce an unwanted relative phase between the horizontal and vertical components in the output polarization state of the sensing network, thereby degrading the performance of weak value amplification. In the following, we present a compensation method to mitigate this relative phase.

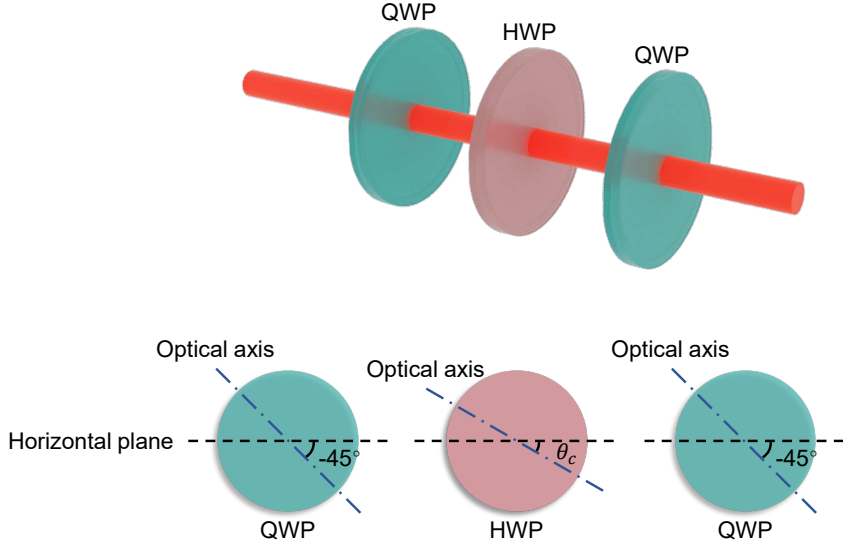


Figure S3. Compensation method for the unwanted relative phase.

Theoretically, the unitary evolution of a single qubit, corresponding to the polarization state in our scheme, belongs to  $SU(2)$ , a three-parameter Lie group that is topologically equivalent to the hypersphere  $S^3$ . A convenient parameterization employs Euler angles: any such unitary can be expressed as a product of three rotations, and can be written as

$$\hat{U}(\varphi, \xi, \zeta) = \hat{R}_y(\varphi)\hat{R}_z(-\xi)\hat{R}_y(\zeta), \quad (S38)$$

with independent real parameters  $(\varphi, \xi, \zeta)$ , and  $\hat{R}_y$  and  $\hat{R}_z$  denote the rotations along  $y$ - and  $z$ -axis, respectively. Since  $SU(2)$  is the double cover of  $SO(3)$ , these operations correspond to rotations of the Bloch (or Poincaré) sphere. Therefore, rotations  $\hat{R}_y$  and  $\hat{R}_z$  are given by

$$\hat{R}_y(\theta) = \cos(\theta)\hat{\mathbb{I}} - i\sin(\theta)\hat{\sigma}_y, \quad \hat{R}_z(\theta) = \cos(\theta)\hat{\mathbb{I}} - i\sin(\theta)\hat{\sigma}_z,$$

where

$$\hat{\sigma}_y = \begin{pmatrix} 0 & -i \\ i & 0 \end{pmatrix}, \quad \hat{\sigma}_z = \begin{pmatrix} 1 & 0 \\ 0 & -1 \end{pmatrix},$$

are the Pauli-Y and Pauli-Z matrix, respectively.

Experimentally, an arbitrary  $SU(2)$  transformation on the polarization state can be realized with the standard QWP–HWP–QWP sequence

$$\hat{U} = \text{QWP}(\eta_1)\text{HWP}(\tau)\text{QWP}(\eta_2),$$

where the arguments denote the respective angles of the plates' fast axes with respect to the horizontal reference, as illustrated in Figure S3.

According to the Jones matrix representation, the operations  $\text{QWP}(\eta)$  and  $\text{HWP}(\tau)$  are given by

$$\text{QWP}(\eta) = \hat{R}_y(\eta)\hat{Q}_0\hat{R}_y(-\eta), \quad \text{HWP}(\tau) = \hat{R}_y(\tau)\hat{H}_0\hat{R}_y(-\tau),$$

where

$$\hat{Q}_0 = \begin{pmatrix} 1 & 0 \\ 0 & i \end{pmatrix}, \quad \hat{H}_0 = \begin{pmatrix} 1 & 0 \\ 0 & -1 \end{pmatrix}.$$

Then the angles of these three wave plates can be obtained as

$$\eta_1 = \varphi - \frac{\pi}{4}, \quad \eta_2 = -\zeta - \frac{\pi}{4}, \quad \tau = \frac{1}{2}(\varphi + \xi - \zeta) - \frac{\pi}{4}.$$

To compensate the unwanted relative phase  $\delta\theta$  introduced by imperfections in the Sagnac interferometer, we implement the compensation operation

$$\hat{U}_c = \hat{R}_z(-\frac{\delta\theta}{2}),$$

which corresponds to Euler-rotation angles

$$\varphi = \zeta = 0, \quad \xi = \frac{\delta\theta}{2}.$$

Accordingly, in the QWP–HWP–QWP configuration, both QWPs are fixed at  $-45^\circ$ , and the HWP is set to  $\delta\theta/4 - 45^\circ$ , thereby canceling the unwanted phase offset.

### Supplementary Note 3: Supplementary Experimental Results

In our experiments, we synchronously applied sinusoidal signals to PZT chips of sensors, and then readout the measured peak SNR at the spectrum analyzer. The peak-to-peak voltages of applied signals vary from 1 mV to 10 mV in 1 mV increments. For each configuration of the sensing network (number of sensors) and applied signal voltage,

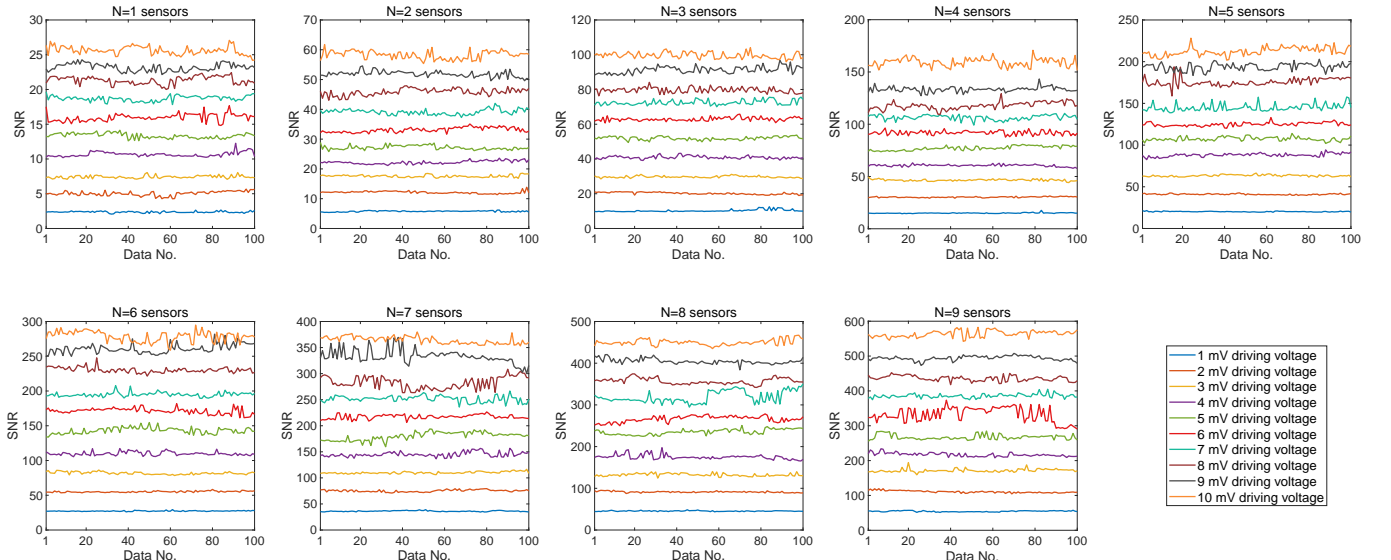


Figure S4. Experimental results of detected SNR. Each subfigure shows results for a different number of sensors in the network. Within each subfigure, the solid curves, ordered from bottom to top, correspond to input signal voltages from 1 mV to 10 mV, respectively, applied at the sensors. Each curve consists of 100 measured data points.

the experiment was repeated 100 times, and the peak SNR at 10 kHz was recorded from the spectrum analyzer. The detailed results are presented in Figure S4.

For each sensing-network configuration (i.e., for a fixed number of sensors), the SNR scales linearly with the applied signal voltage, and this linear relation can be determined from the experimental data presented above. Imposing  $\text{SNR} = 1$  defines the minimum applicable voltage  $V_{\min}^{(\text{PZT})}$  for the PZT chips of sensors, which corresponds to the experimentally determined minimum detectable average tilt angle,  $\delta\bar{\varphi}_{\min}^{(\text{det})}$ . The detailed results are listed in Table S1.

Table S1. Experimental results of detected precision.

| Number of sensors  | 1                   | 2                   | 3                   | 4                   | 5                   | 6                  | 7                  | 8                  | 9                  |
|--|---------------------|---------------------|---------------------|---------------------|---------------------|--------------------|--------------------|--------------------|--------------------|
| $V_{\min}^{(\text{PZT})}$ <sup>a</sup>                   | 382.6 $\mu\text{V}$ | 175.3 $\mu\text{V}$ | 98.6 $\mu\text{V}$  | 65.5 $\mu\text{V}$  | 46.8 $\mu\text{V}$  | 35.5 $\mu\text{V}$ | 27.6 $\mu\text{V}$ | 22.2 $\mu\text{V}$ | 18.1 $\mu\text{V}$ |
| $\delta\bar{\varphi}_{\min}^{(\text{det})}$ <sup>b</sup> | 841.8 $\text{prad}$ | 385.7 $\text{prad}$ | 217.0 $\text{prad}$ | 144.1 $\text{prad}$ | 103.1 $\text{prad}$ | 77.7 $\text{prad}$ | 60.6 $\text{prad}$ | 48.9 $\text{prad}$ | 39.8 $\text{prad}$ |

<sup>a</sup> Minimal peak-to-peak voltages of signals applied to sensors, corresponding to detected  $\text{SNR} = 1$  at the spectrum analyzer.

<sup>b</sup> Minimal detectable average tilt angles in experiments.